

High-throughput discovery of novel developmental phenotypes

Mary E. Dickinson^{1*}, Ann M. Flenniken^{2,3*}, Xiao Ji^{4*}, Lydia Teboul^{5*}, Michael D. Wong^{2,6*}, Jacqueline K. White⁷, Terrence F. Meehan⁸, Wolfgang J. Weninger⁹, Henrik Westerberg⁵, Hibret Adissu^{2,10}, Candice N. Baker¹¹, Lynette Bower¹², James M. Brown⁵, L. Brianna Caddle¹¹, Francesco Chiani¹³, Dave Clary¹², James Cleak⁵, Mark J. Daly^{14,15}, James M. Denegre¹¹, Brendan Doe⁷, Mary E. Dolan¹¹, Sarah M. Edie¹¹, Helmut Fuchs¹⁶, Valerie Gailus-Durner¹⁶, Antonella Galli⁷, Alessia Gambadoro¹³, Juan Gallegos¹⁷, Shiyang Guo¹⁸, Neil R. Horner⁵, Chih-Wei Hsu¹, Sara J. Johnson⁵, Sowmya Kalaga¹, Lance C. Keith¹, Louise Lanoue¹², Thomas N. Lawson⁵, Monkol Lek^{14,15}, Manuel Mark¹⁹, Susan Marschall¹⁶, Jeremy Mason⁸, Melissa L. McElwee¹, Susan Newbigging^{2,10}, Lauryl M. J. Nutter^{2,10}, Kevin A. Peterson¹¹, Ramiro Ramirez-Solis⁷, Douglas J. Rowland¹², Edward Ryder⁷, Kaitlin E. Samocha^{14,15}, John R. Seavitt¹⁷, Mohammed Selloum¹⁹, Zsombor Szoke-Kovacs⁵, Masaru Tamura²⁰, Amanda G. Trainor¹², Ilinca Tudose⁸, Shigeharu Wakana²⁰, Jonathan Warren⁸, Olivia Wendling¹⁹, David B. West²¹, Leeyean Wong¹, Atsushi Yoshiki²⁰, The International Mouse Phenotyping Consortium†, Daniel G. MacArthur^{14,15}, Glauco P. Tocchini-Valentini¹³, Xiang Gao¹⁸, Paul Flicek⁸, Allan Bradley⁷, William C. Skarnes⁷, Monica J. Justice^{10,17}, Helen E. Parkinson⁸, Mark Moore²², Sara Wells⁵, Robert E. Braun¹¹, Karen L. Svenson¹¹, Martin Hrabe de Angelis^{16,23,24}, Yann Hérault¹⁹, Tim Mohun²⁵, Ann-Marie Mallon⁵, R. Mark Henkelman^{2,6}, Steve D. M. Brown⁵, David J. Adams⁷, K. C. Kent Lloyd¹², Colin McKerlie^{2,10}, Arthur L. Beaudet¹⁷, Maja Bucan²⁶ & Stephen A. Murray¹¹

Approximately one third of all mammalian genes are essential for life. Phenotypes resulting from knockouts of these genes in mice have provided tremendous insight into gene function and congenital disorders. As part of the International Mouse Phenotyping Consortium effort to generate and phenotypically characterize 5,000 knockout mouse lines, we have identified 410 lethal genes during the production of the first 1,751 unique gene knockouts. Using a standardized phenotyping platform that incorporates high-resolution 3D imaging, we identified phenotypes at multiple time points for previously uncharacterized genes and additional phenotypes for genes with previously reported mutant phenotypes. Unexpectedly, our analysis reveals that incomplete penetrance and variable expressivity are common even on a defined genetic background. In addition, we show that human disease genes are enriched for essential genes identified in our screen, thus providing a data set that facilitates the prioritization and validation of mutations identified in clinical sequencing efforts.

Our understanding of the genetic mechanisms required for normal embryonic growth and development has been advanced by the analysis of single mutations generated in individual labs or by the identification of mutants through focused mutagenesis screens^{1–4}. Systematic, standardized approaches to mouse phenotypic analysis complement these data, capitalizing on the efficiency provided by scale and reducing the potential for ascertainment bias, and ultimately providing a means to achieve genome-wide functional annotation. Moreover, recent challenges relating to the reproducibility of animal model experiments^{5,6} emphasize the need for careful standardization of allele design, genetic background and phenotyping protocols. Building on these principles,

the goal of the International Mouse Phenotyping Consortium (IMPC) is to generate a catalogue of gene function by systematically generating and phenotyping a genome-wide collection of gene knockouts in mice. To date, nearly 5,000 new knockout lines have been created by IMPC using the International Knockout Mouse Consortium (IKMC) resources^{7–12}. Here, we report the results of an international, systematic effort to identify and characterize the phenotypes of embryonic lethal mutations using a standardized¹³, high-throughput pipeline. These findings provide insights into gene function, represent potential models for inherited disorders and shed further light on the role of essential genes in a variety of monogenic and complex human disorders.

¹Department of Molecular Physiology and Biophysics, Houston, Texas 77030, USA. ²The Toronto Centre for Phenogenomics, Toronto, Ontario M5T 3H7, Canada. ³Mount Sinai Hospital, Toronto, Ontario M5T 3H7, Canada. ⁴Genomics and Computational Biology Program, Perelman School of Medicine, University of Pennsylvania, Philadelphia, Pennsylvania 19104, USA. ⁵Medical Research Council Harwell (Mammalian Genetics Unit and Mary Lyon Centre), Harwell, Oxfordshire OX11 0RD, UK. ⁶Mouse Imaging Centre, The Hospital for Sick Children, Toronto, Ontario M5G 1X8, Canada. ⁷The Wellcome Trust Sanger Institute, Wellcome Trust Genome Campus, Hinxton, Cambridge CB10 1SA, UK. ⁸European Molecular Biology Laboratory, European Bioinformatics Institute, Wellcome Trust Genome Campus, Hinxton, Cambridge CB10 1SD, UK. ⁹Centre for Anatomy and Cell Biology, Medical University of Vienna, Vienna A-1090, Austria. ¹⁰The Hospital for Sick Children, Toronto, Ontario M5G 0A4, Canada. ¹¹The Jackson Laboratory, Bar Harbor, Maine 04609, USA. ¹²Mouse Biology Program, University of California, Davis, California 95618, USA. ¹³Monterotondo Mouse Clinic, Italian National Research Council (CNR), Institute of Cell Biology and Neurobiology, Monterotondo Scalo I-00015, Italy. ¹⁴Analytic and Translational Genetics Unit, Massachusetts General Hospital, Boston, Massachusetts 02114, USA. ¹⁵Program in Medical and Population Genetics, Broad Institute MIT and Harvard, Cambridge, Massachusetts 02142, USA. ¹⁶Helmholtz Zentrum München, German Research Center for Environmental Health, Institute of Experimental Genetics and German Mouse Clinic, Neuherberg 85764, Germany. ¹⁷Department of Molecular and Human Genetics, Baylor College of Medicine, Houston, Texas 77030, USA. ¹⁸SKL of Pharmaceutical Biotechnology and Model Animal Research Center, Collaborative Innovation Center for Genetics and Development, Nanjing Biomedical Research Institute, Nanjing University, Nanjing 210061, China. ¹⁹Infrastructure Nationale PHENOMIN, Institut Clinique de la Souris (ICS), et Institut de Génétique Biologie Moléculaire et Cellulaire (IGBMC) CNRS, INSERM, University of Strasbourg, Illkirch-Graffenstaden 67404, France. ²⁰RIKEN BioResource Center, Tsukuba, Ibaraki 305-0074, Japan. ²¹Children's Hospital Oakland Research Institute, Oakland, California 94609, USA. ²²IMPC, San Anselmo, California 94960, USA. ²³Chair of Experimental Genetics, School of Life Science Weihenstephan, Technische Universität München, Freising 81675, Germany. ²⁴German Center for Diabetes Research (DZD), Neuherberg 85764, Germany. ²⁵The Francis Crick Institute Mill Hill Laboratory, The Ridgeway, Mill Hill, London NW1 1AT, UK. ²⁶Departments of Genetics and Psychiatry, Perelman School of Medicine, University of Pennsylvania, Philadelphia Pennsylvania 19104, USA.

†A list of participants and their affiliations appears at the end of the paper.

*These authors contributed equally to this work.

Discovery of mouse essential genes

Intercrosses of 1,751 germ line-transmitted (GLT) heterozygous lines from IMPC production colonies¹ identified 410 lines that displayed lethality (Fig. 1a), defined as the absence of homozygous mice after screening of at least 28 pups ($P < 0.001$ Fisher's exact test) before weaning. We also identified 198 'subviable' lines, defined as fewer than 12.5% (half of expected) homozygous preweaning pups (full list of genes available in Supplementary Table 1). The vast majority of the alleles investigated in this study were IKMC variants that disrupt the coding sequence and remove the neomycin resistance cassette (1,704 of 1,804 unique alleles; see Extended Data Fig. 1 for a schematic of each allele and Supplementary Table 2 for all other alleles investigated). The proportion of essential genes varied between centres and ranged from 4.8% to 52.7%. This probably reflects the different biases in gene selection criteria between centres and specific consortium arrangements for lethal gene characterization (Extended Data Fig. 2a, b). No significant bias was observed in the distribution of lethal genes across mouse chromosomes (Extended Data Fig. 2c, d). Overall, the lethal proportion (23.4%) was consistent with published observations of null alleles^{7,9,12,13}, particularly when combined with subviable lines (11.3%), resulting in 65.3% overall viability for IMPC knockout lines. A main goal of this project was to provide phenotype data for unknown or novel genes, that is, those genes with no prior reports of a targeted null allele in the mouse, as curated in Mouse Genome Informatics (MGI). The primary viability data indicated that such unannotated genes displayed an overall viability rate of 66.5%, compared to the 62% viability rate among previously reported null alleles (Extended Data Fig. 2e; novel versus prior gene lists can be found in Supplementary Table 3; list of all first publications or reports of gene knockouts can be found in Supplementary Table 4). These data reveal consistent identification of essential genes in our program and further support the finding that approximately 35% (24% lethal and 11% subviable) of null mutations across the genome are for genes that are essential for survival at normal Mendelian ratios.

Functional data from knockouts in mice are highly informative, and thus would be predicted to have a strong impact on Gene Ontology Consortium¹⁴ annotations. For the 1,751 IMPC knockout mouse lines phenotyped to date, IMPC phenotyping provides the only experimental evidence for over 40% of the genes in the data set. Using the GOSlim tool, which clusters terms associated with each gene into a set of broad categories, we observed enrichment in lethal and subviable genes

within several categories (Extended Data Fig. 3). Compared to novel genes, the number of annotations for the majority of process and function categories was greater for published alleles, highlighting the value of our analysis in assigning function to novel, previously uncharacterized genes.

We used data from three recent publications on genome-wide screens for cell-essential genes in human cells to address the overlap between essential genes in the human and mouse genome^{15–17}. We selected core essential human genes from each study and compared these to the human orthologues of mouse essential genes on the consensus list of curated IMPC-MGI genes. We found that approximately 35% of core essential genes in each study were associated with lethality or subviability in the mouse, and that 61–62% of genes were currently unknown (Fig. 1b). Of the 19 human essential genes common to all three studies that were nonessential in the mouse, only three (*Rbmx*, *Dkc1*, and *Sod1*) could reliably be confirmed as a targeted knockout of a nonessential gene, highlighting the remarkable concordance between mouse and human in their core essential genes.

To expand the depth of our analysis of essential genes, we developed a comprehensive phenotyping pipeline¹³ designed to identify the time of lethality, assign phenotypes and document LacZ expression patterns at discrete time points (Extended Data Fig. 4). A key aspect of the pipeline is the incorporation of optical projection tomography (OPT)¹⁸, micro-computed tomography (micro-CT)^{19–21} and high-resolution episcopic microscopy (HREM)²², which provide cost-effective, high-throughput approaches to the collection of phenotype data, including quantitative volumetric analysis (see below). The catalogue of knockout lines and all phenotype data are available to the community via the IMPC portal (www.mousephenotype.org).

Using a tiered strategy, we established clear viable versus lethal (defined if homozygous embryos were absent or lacked a heartbeat) calls at up to four different time points for a total of 283 lethal lines; the total number of lethal lines varied by progress through the pipeline (a comprehensive progress table for all 1,861 alleles is provided in Supplementary Table 5). From these data, we established windows of lethality for 242 genes with complete data to more precisely define the timing of embryonic death. Figure 1c shows that the majority of lines (147/242; 60.7%) died before E12.5 and in the majority of these early lethal lines (107/147; 72.8%) development ceased before E9.5, the earliest time point examined. Remarkably, only nine total lines died in

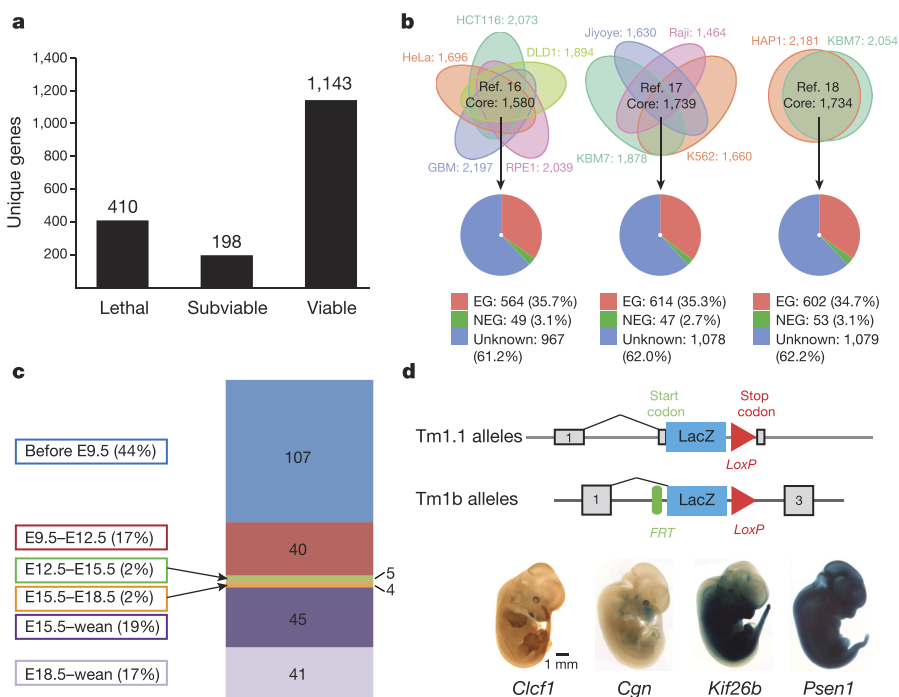


Figure 1 | Large-scale identification of essential genes. **a**, Number of viable, subviable and lethal genes identified from intercrosses of IMPC knockout alleles. **b**, Core essential human genes identified in three studies: 1,580¹⁶, 1,739¹⁷, and 1,734¹⁵ (top row) (see Methods). Pie charts indicate overlap between core human cell-essential genes and orthologous genes in the mouse: essential (EG, red); non-essential (NEG, green) and genes with unknown function in the mouse (Unknown, blue). **c**, Numbers and percentages of 242 IMPC lines showing lethality within a particular temporal window. **d**, IMPC allele structure showing LacZ reporter (top). Specific LacZ expression for *Clcf1*, *Cgn*, *Kif26b* and widespread expression shown for *Psen1* (bottom). Scale bar, 1 mm.

the E12.5–E15.5 or E15.5–E18.5 windows, while most lines that were viable at E12.5 were also viable at the latest time point examined (E15.5 or E18.5). Although viable, many of these lines showed phenotypes at E15.5 and E18.5 (see below), and ultimately died in the perinatal or early postnatal period.

Taking advantage of the LacZ cassette present in most IMPC alleles^{10,11}, gene expression was evaluated in heterozygous embryos at E12.5 in the lethal or subviable lines. Expression patterns fell into three broad categories as shown in Fig. 1d (bottom): restricted (for example, *Clcf1*, *Cgn* and *Kif26b*); ubiquitous (for example, *Psen1*); or undetectable expression (not shown). All images and annotations of the expression atlas are available at the IMPC portal, providing a rich and growing *in situ* expression atlas for the scientific community.

Identification of lethal phenotypes

At each time point, gross morphological phenotypes were recorded using a structured set of Mammalian Phenotype terms (Supplementary Table 6). An analysis of phenotype areas revealed that the most common phenotype overall was growth and developmental delay (Fig. 2a–c) affecting 23.5%, 44.1% and 39.3% of lines at E12.5, E14.5–E15.5 and E18.5, respectively. Abnormalities in cardiovascular development were also common, frequently observed at both E12.5 and E15.5 (Fig. 2a, b), along with craniofacial malformations and defects in development of the limbs and/or tail. At E18.5, a number of mutants exhibited respiratory and/or body wall abnormalities (captured as ‘other’), in addition to the growth abnormalities seen at other stages.

Our pipeline has identified a number of potentially novel phenotypes for previously unreported knockouts. In all cases, 3D imaging revealed additional phenotypes that might have been missed by gross inspection. For example, *Tmem132a* E15.5 homozygous embryos were smaller than their littermates and displayed obvious spina bifida and narrow, club-shaped limbs (Fig. 2d, f). Sagittal cross-sections through the micro-CT data showed abnormal curvature in the spinal column adjacent to the open neural tube and an abnormal head structure in mutants (Fig. 2e, g). Kidney defects were also observed in E15.5 mutant embryos ($n = 3$) and bladder defects were also evident by E18.5 ($n = 4$) (not shown). *Svep1* homozygous mutant embryos displayed multiple defects at both E15.5 and E18.5, including severe oedema and discolouration (Fig. 2h, k) and died in the perinatal period. Additionally, transverse sections of micro-CT data from E18.5 embryos revealed abnormal development of the kidney pelvis (Fig. 2i, l), severely hypoplastic lungs and a thin myocardium (Fig. 2j, m). Homozygous *Klhdc2* embryos at E14.5 displayed hind limb preaxial polydactyly (Fig. 2n, q arrow) and oedema (Fig. 2n, q (arrowhead)). Sections of micro-CT volumes additionally revealed hypoplastic adrenal glands (Fig. 2s), displaced kidneys, a shorter tongue, and abnormal intestines (Fig. 2r).

A number of mutants with impaired cardiovascular function were identified (Fig. 2a–c), including *Strn3*, *Atg3*, and *Slc39a8* (Extended Data Fig. 5). Similarly, cardiovascular defects were common at E9.5, as illustrated in detail using OPT (for example, *Tmem100*, Extended Data Fig. 6). OPT data sets can be manipulated in three dimensions to reveal additional phenotypes such as abnormal neural tube closure,

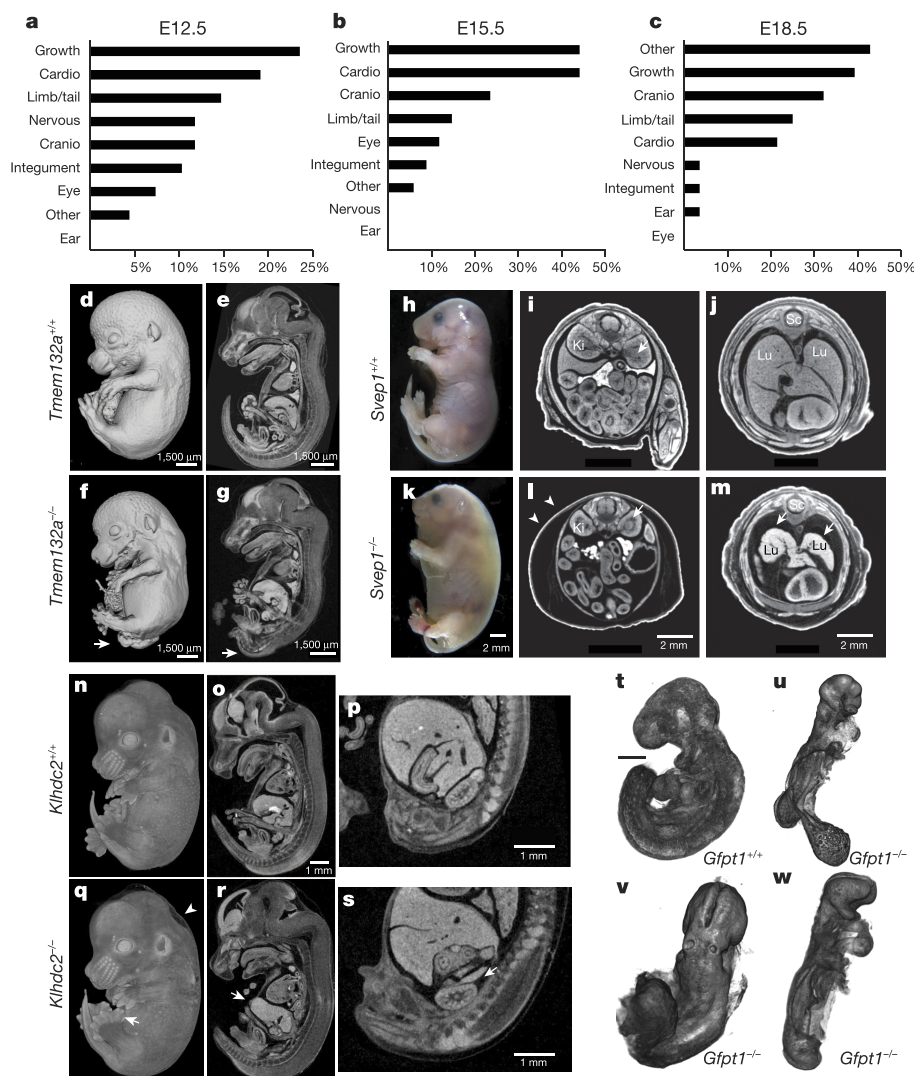


Figure 2 | Systematic identification of novel embryonic phenotypes. a–c, Frequency of gross morphological phenotypes at E12.5 (a), E15.5 (b) and E18.5 (c) (Supplementary Table 6).

d–g, Spina bifida in E15.5 *Tmem132a* knockout embryos (arrow) ($n = 4$ mutants), as well as narrow limbs with fewer digits ($n = 5$ mutants). Scale bars, 1,500 μm. h–m, Gross morphology of E18.5 *Svep1* knockout embryos reveals severe oedema (k versus h; white arrowheads). Transverse views reveal an abnormal renal pelvis (i versus l, arrow), hypoplastic lungs, and thin myocardium (arrows in m versus j). Lu, lungs; Ki, kidneys; Sc, spinal cord ($n = 14$ mutants). Scale bars, 2 mm. n–s, Mutant (q) E14.5 *Klhdc2* embryos show polydactyly (arrow) and oedema (arrowhead) versus controls (n). Sagittal views revealed a thin body wall (arrow in r) and missing adrenal glands (s) (E14.5, $n = 2$; E18.5, $n = 3$). Scale bars, 1 mm. t–w, E9.5 OPT surface renderings show abnormal allantois development (u), failure to complete turning (u–w) and abnormal heart looping (w) in mutant *Gfpt1* embryos ($n = 4$ mutants).

3

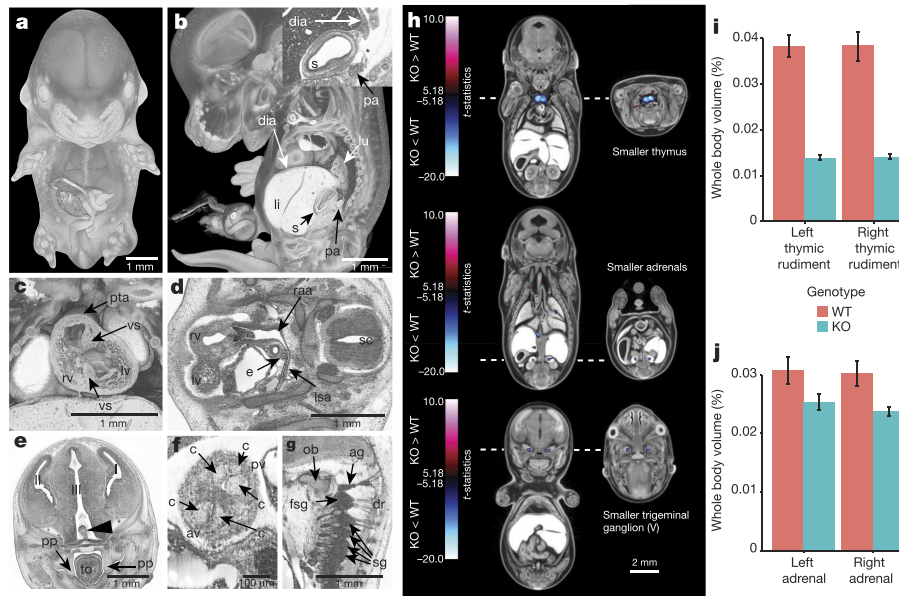


Figure 3 | Deep phenotyping through high-resolution 3D imaging and quantitative volumetric analysis. a–g, Phenotypic features of *Chtop* null embryos identified by HREM imaging ($n = 4$ mutants analysed). a, 3D surface model of a mutant embryo. Scale bar, 1 mm. b, Sagittal view, revealing abnormal topology of pancreatic tissue (pa). Scale bar, 1 mm. Insert shows stomach (s) with a defect in the formation of the diaphragm (dia) (asterisk). Lu, lung; li, liver. c, Coronal plane to reveal double outlet right ventricle (rv), persisting truncus arteriosus (pta), and ventricle septum defects (vs). Lv, left ventricle. Scale bar, 1 mm. d, Transverse section showing defects in the right aortic arch (raa) and retroesophageal left subclavian artery (lsa). E, oesophagus; sc, spinal cord. Scale bar, 1 mm. e, Coronal section showing neural tissue (arrowhead) abnormally protruding into the 3rd brain ventricle (III), and unelevated palatine plates (pp). I, 1st brain ventricle and left telencephalon; II, 2nd brain ventricle

and right telencephalon; tongue (to). Scale bar, 1 mm. f, Coronal section showing bicuspid aortic valve (av). C, cusp of semilunar valve; pulmonary valve (pv). Scale bar, 1 mm. g, Sagittal section showing fused spinal ganglia (fsg) and additional ganglion material (ag) caudal to the occipital bone (ob) ($n = 2$ out of 4 embryos). Sg, spinal ganglion; dr, dorsal roots of spinal nerve. Scale bar, 1 mm. h, Coronal and transverse sections through composites of *Cbx4*^{-/-} embryos registered to an average control data set. Blue, smaller volumes in the mutant; red, larger volumes. The blue clusters in the top panel correspond to the smaller right and left thymic rudiments, the adrenal glands in the middle panel, and the trigeminal ganglia (V) in the bottom panel. Scale bar, 2 mm. i, Whole structural volume differences for the left and right thymic rudiment. j, Whole structural volume differences for the adrenal glands. Error bars represent 95% confidence intervals ($n = 8$ mutants for h–j).

turning and chorion–allantois fusion, as seen in homozygous *Gfpt* mutant embryos (Fig. 2t–w).

Chtop mutant embryos showed obvious developmental delay, neural tube defects, craniofacial dysmorphology, abnormal eye development and subcutaneous oedema. HREM was used to define further defects at E14.5, revealing major abnormalities in the ribs and vertebrae, the cardiovascular system and the nervous system at a spatial resolution rivalling standard histological techniques (Fig. 3a–g).

In addition to manual annotation, 3D images are amenable to automated computational analyses that can identify mutant anatomical phenotypes that are statistically different from wild-type variation^{19,20}. As an example, prior studies of *Cbx4*-knockout mice revealed a clear hypoplastic thymus²³. Automated volumetric analysis of E15.5 *Cbx4*-null mice generated by the IMPC replicated these findings, but also revealed adrenal hypoplasia and smaller trigeminal ganglia using deformation-based morphometry and a 3D segmented mouse embryo atlas (Fig. 3h–j). This analysis also identified a smaller cochlea in *Eya4* mutants, directing more in-depth histopathology analysis to the affected region (Extended Data Fig. 6).

Some centres have expanded the pipeline to include analyses of lines that are lethal between birth and weaning, employing tools such as whole brain MRI. These analyses have identified previously unknown phenotypes for *Tox3* at P7, including a smaller cerebellum displaying hypoplasia and dysplasia, and an absent transient external granular layer (Extended Data Fig. 7). Similar analysis of *Rsph9*, a gene associated with primary ciliary dyskinesia in humans (OMIM #612650), has identified a potential mouse model of this disease. All P7 homozygous mice showed enlarged ventricles, while histopathology revealed severe triventricular hydrocephalus with marked rarefaction, cavitation and loss of periventricular cortical tissue as well as severe sinusitis, which is typical of ciliary dysfunction (Extended Data Fig. 8).

Subviable genes and incomplete penetrance

Unexpectedly, we observed instances of phenotypes that displayed incomplete penetrance, including variable lethality (subviability), despite the standard allele structure and defined genetic background. Prior work has shown that lethal genes are much less likely than viable genes to have a paralogue, and thus have less potential for functional redundancy¹². Genes from subviable lines, by contrast, were more likely to have a paralogue, similar to viable lines (Fig. 4a). This is consistent with a model in which incomplete penetrance and variable expressivity²⁴ are due to cell-autonomous, stochastic variation in gene expression in components of disrupted ‘buffered’ pathways^{25,26}, where paralogues may provide functional redundancy. For example, two alleles of the *Acvr2a* gene have been generated on a mixed genetic background^{27,28} and both display variable phenotypes including partial lethality. On a uniform C57BL/6N background we also observed subviability and a wide range of morphological phenotypes at E15.5 including a small or missing mandible, cyclopia and holoprosencephaly (Fig. 4b–i); this is consistent with the normal assembly of *Acvr2a* into a heteromeric signalling complex with its paralogue *Acvr2b*. Other examples include *Rab34*, which has three paralogues in the RAB protein family (*Rab6a*, *Rab6b* and *Rab36*). In addition to the consistent phenotypes of polydactyly and lung hypoplasia, *Rab34* mutants also display highly variable craniofacial malformations, haemorrhage, oedema and exencephaly (Fig. 4j–m).

For all cases of lethal and subviable genes, full cohorts of heterozygous mice were phenotyped as part of the IMPC Adult Phenotyping pipeline, along with surviving subviable homozygous mice in some cases. Viable homozygous mice displayed a greater number of phenotype hits per gene than heterozygous mice from the lethal class, although the average difference was only 1.44 more hits (Extended Data Fig. 9a). However, subviable mice homozygous for a null allele averaged 5.8 hits

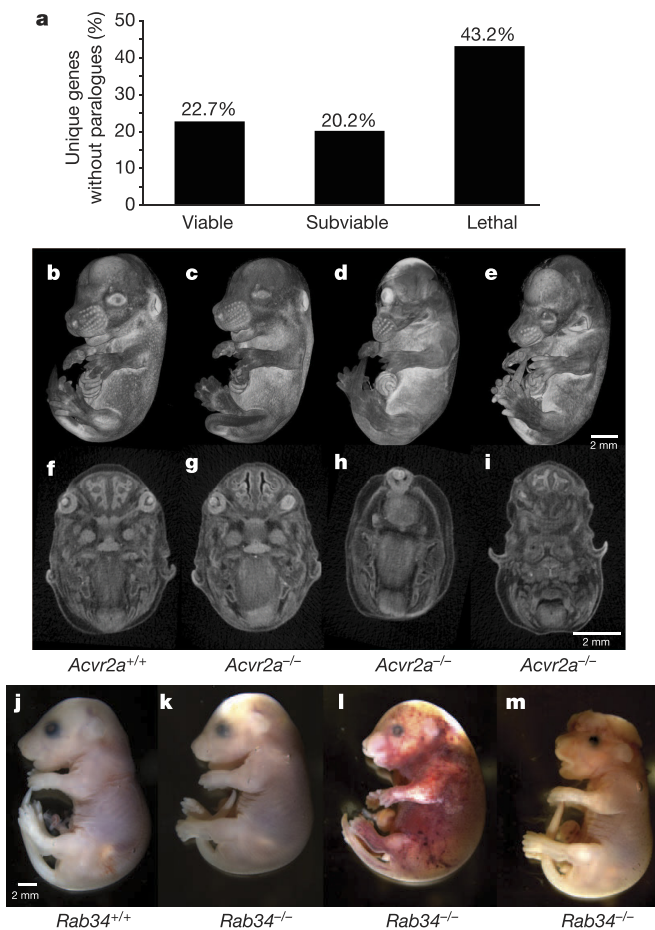


Figure 4 | Frequent instances of subviability, incomplete penetrance, and variable expressivity in a uniform genetic context. **a**, Comparison of the total percentage of unique genes that lack a paralogue between viable, subviable, and lethal phenotypes. **b–e**, Surface renderings (**b–e**) and transverse sections of the heads (**f–i**) of E15.5 *Acvr2a*^{-/-} embryos reveal a range of phenotypes ($n = 8$ mutants). **j–m**, Variable expressivity of phenotypes is observed in *Rab34* mutant embryos at E18.5 ($n = 7$ mutants). Scale bar, 2 mm.

per line compared to an average of 4.0 hits per line for homozygote and hemizygote viable lines (Extended Data Fig. 9b).

Novel insights into functions of human disease genes

It has been shown that genes causing lethality in mice are enriched in disease genes^{29,30}. We established orthology between genes in mice and humans, and used the Human Genome Mutation Database (HGMD) to annotate human disease associations^{31,32}. We next compiled an updated list of 3,326 essential genes by combining the published data from the MGI database (mammalian phenotype terms listed in Supplementary Table 7) and 608 genes identified in the IMPC effort as causing lethality and subviability, along with 4,919 nonessential genes. With these updated lists, we report an even stronger enrichment of essential genes relative to nonessential for human disease genes catalogued in the HGMD (odds ratio = 2.00, $P = 6.83 \times 10^{-39}$, Fig. 5a). Consistent with this enrichment, of the 3,302 protein-coding HGMD disease genes, 2,434 have a reported phenotype and more than half (1,253) are essential in mice (Fig. 5b; Supplementary Table 8). Furthermore, we found an enrichment of essential genes in comparison to nonessential genes (odds ratio = 1.16, $P = 0.0015$) among 6,384 genes encompassing or neighbouring the disease- and trait-associated variants in the NHGRI-EBI catalogue of published genome-wide association studies ('GWAS hits')³³ (Fig. 5c).

The IMPC effort expanded a phenotypic spectrum for over 300 genes associated with known Mendelian diseases. From 194 subviable genes

with identified human orthologues, 57 were associated with human disease, of which 34 were previously unreported for their subviable phenotypes (Supplementary Table 9; new reports indicated by 'N' in column J). For example, SET binding protein 1 (*SETBP1*) has been reported as frequently mutated in several types of chronic leukaemia and in Schnitzel-Giedion syndrome, a congenital disease characterized by a high prevalence of tumours, severe mid-face hypoplasia, heart defects and skeletal anomalies^{34,35}. Among 399 lethal genes, 126 human orthologues have been associated with human diseases, including 52 disease genes for which our data provide the first report of their null phenotype in the mouse (Supplementary Table 10). The human orthologues of these novel lethal genes have been linked to metabolic and storage syndromes (*ADSL*, *DHFR*, *GYGI*, *PC*), mitochondrial complex deficiencies (*ATP5E*, *NDUFS1*, *NUBPL*, *SDHA*, *SLC25A3*, *UQCRLB*), or syndromes caused by disruption of basic processes such as replication or translation initiation (*EIF2B3*, *EIF2B4*, *ORC1*). The severity of clinical manifestation of these human syndromes ranges from neonatal lethality (*BBS10*, *SLC25A3*) matching the observed phenotype in the mouse, to neurological disorders and intellectual disability (*COQ6*, *DEPDC5*, *GOSR2*, *KDM5C*, *YARS*). These differences in clinical manifestation may be due to differences between underlying biological processes in the mouse and human. Alternatively, a different set of alleles, rather than null, may underlie these dominant or recessive human syndromes. *GYGI* mutations have been found in patients with glycogen storage disease XV (GSD15; 613507, ref. 36), and in an additional seven patients with polyglucosan body myopathy 2 (PGBM2; 616199). Both diseases affect the skeletal muscle, but PGBM2 is characterized by polyglucosan accumulation in the muscle and skeletal myopathy without cardiac involvement³⁷. Homozygous *Gyg* null embryos die perinatally and show severe heart abnormalities consistent with cardiac hypertrophy evident as early as E15.5 (Fig. 5d, e). At E12.5, LacZ expression was detected specifically in the heart and the carotid and umbilical arteries, correlating strongly with the heart phenotype and heart abnormalities in GSD15 patients (Fig. 5f). Micro-CT images at E18.5 revealed an enlargement of the thymus as well as abnormal morphology of the brain and spinal cord consistent with degeneration (Extended Data Fig. 10a–h). *Gyg* mutations have not previously been reported in the mouse and this model will be valuable for understanding the distinct roles of *Gyg* in different organs and potentially for understanding the consequences of different alleles in patients. In another example, for a human syndrome arising from a chromosomal deletion (16p) (ref. 38), *Kdm8* was indicated as a strong candidate amongst a pool of candidate genes in our screen (Extended Data Fig. 10i–t).

We also used the updated catalogue of mouse essential and nonessential genes to compare the mutability of their human orthologues in exome sequences of 60,706 subjects in the Exome Aggregation Consortium data (ExAC, <http://exac.broadinstitute.org> and ref. 39). The ExAC data were used to generate intolerance scores for all protein-coding genes by two complementary methods: a) the residual variation intolerance score (RVIS), which is based on intolerance to common missense and truncating single nucleotide variation⁴⁰; and b) the estimation of probability of being loss of function intolerant (pLI score) (ExAC). Human orthologues of essential genes are more intolerant to variation (low RVIS and high pLI scores) than orthologues of nonessential genes and all genes in the human genome ($P < 2.2 \times 10^{-16}$ for lower percentiles in essential genes using the two scoring systems, Fig. 5g, h). Moreover, the IMPC effort identified a set of 22 human orthologues of essential genes that were not previously associated with human disease (Fig. 5i; Supplementary Table 11), but based on their intolerance to functional variation and lethality of their null alleles in the mouse they represent strong candidates for undiagnosed human diseases.

Discussion

In this study, we have described the systematic characterization of embryonic lethal phenotypes as part of a collaborative effort to generate a genome-wide catalogue of gene function. A unique aspect of our

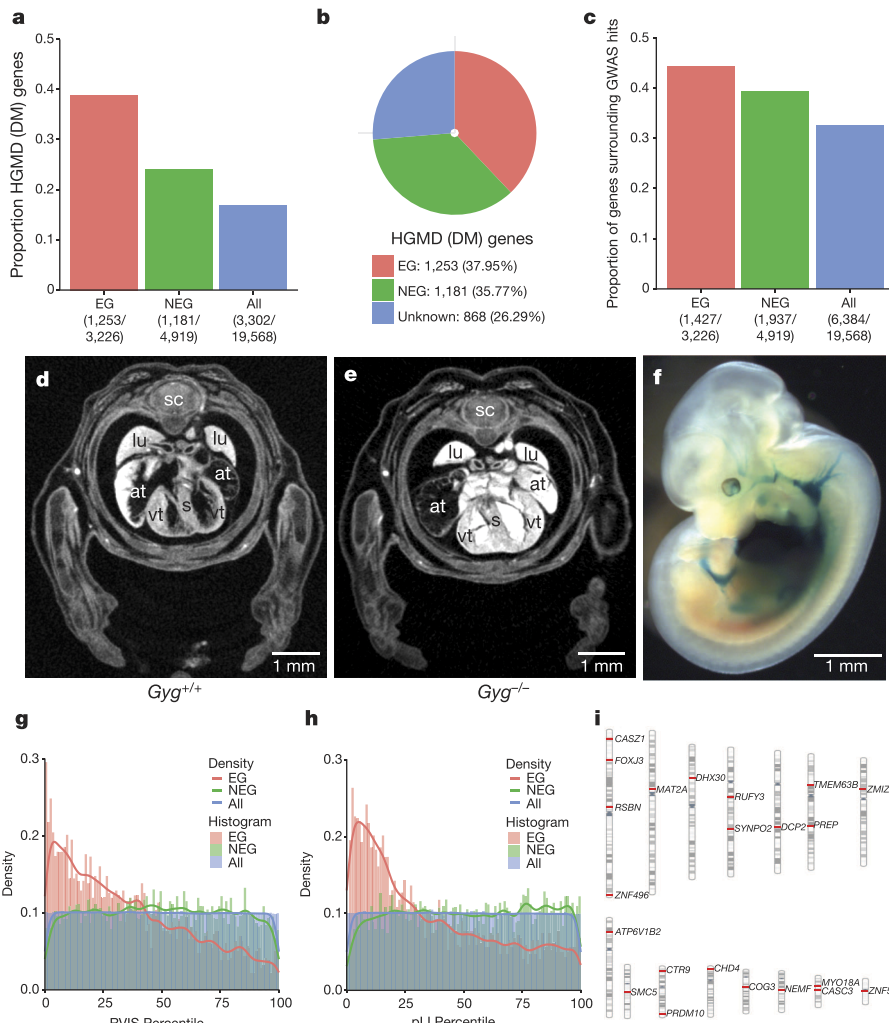


Figure 5 | Essential genes are enriched in human disease genes and intolerant to genetic variation.

a, The fractions indicate the number of HGMD disease genes (disease-causing mutations (DM)) ($n = 3,302$) among 3,326 essential genes (EG, red); 4,919 nonessential genes (NEG, green) and 19,568 protein-coding genes (All, blue). Fisher's exact test for enrichment: EG versus NEG (odds ratio = 2.00, $P = 7.80 \times 10^{-46}$), EG versus All (odds ratio = 3.13, $P = 2.42 \times 10^{-160}$), NEG versus All (odds ratio = 1.56, $P = 1.83 \times 10^{-29}$).

b, Essentiality status of 3,302 HGMD disease genes. **c**, The fractions indicate the number of genes encompassing or neighbouring GWAS hits³³ ($n = 6,384$) divided by essentiality status. Fisher's exact test for enrichment: EG versus NEG (odds ratio = 1.16, $P = 0.0015$), EG versus All (odds ratio = 1.56, $P = 5.80 \times 10^{-31}$), NEG versus All (odds ratio = 1.35, $P = 1.18 \times 10^{-19}$).

d, e, *Gyg* null embryos at E15.5 show enlarged atria (at) and a thickened ventricular wall versus controls. Scale bars, 1 mm. **f**, LacZ expression for *Gyg* was seen in the heart and vascular system (homozygote shown). Scale bar, 1 mm. **g**, Distribution of percentiles of the residual variation intolerance score (RVIS) across three classes of genes: EG, NEG and All. Wilcoxon rank-sum test: EG versus NEG ($P < 2.2 \times 10^{-16}$), EG versus All ($P < 2.2 \times 10^{-16}$), NEG versus All ($P = 0.579$).

h, Distribution of percentiles of the probability of being loss of function intolerant (pLI) across three classes of genes: EG, NEG and All. Wilcoxon rank-sum test: EG versus NEG ($P < 2.2 \times 10^{-16}$), EG versus All ($P < 2.2 \times 10^{-16}$), All versus NEG ($P = 4.15 \times 10^{-5}$).

i, Chromosomal distribution of 22 human orthologues of RVIS and pLI intolerant essential genes that are not currently included in the catalogues of Mendelian disease genes.

pipeline is the incorporation of high-resolution, high-throughput 3D imaging methods, affording detailed morphological information and automated analysis¹⁹. High-resolution data sets are available to the community through a common portal, facilitating additional, in-depth analysis by other investigators that will further enrich the phenotype calls reported in the primary screen. These data are provided in real time, without embargo, to create an 'open access' environment that allows investigators to rapidly evaluate new models. Importantly, open availability of the mouse models themselves reduces the cost and time lost through duplication of effort¹⁹.

Beyond the direct benefit to understanding gene function, this resource has significant relevance to disease-causing genes in humans. We found that the human orthologues of mouse essential genes show evidence of purifying selection in the human population, suggesting a common intolerance to mutation in both mouse and humans. Recent work has identified cases of homozygous loss of function in the human population^{41,42}, complementing on-going efforts to discover disease genes in highly consanguineous populations, including mutations that are homozygous lethal^{43,44} (D.S., personal communication).

Overall, the data presented here illustrate a rich resource with implications for many scientific communities. The high efficiency and reduced cost of CRISPR/Cas9 technology⁴⁵ will allow the IMPC to further expand its coverage of the mammalian genome, and additionally provide a means to target genes and sequence features not currently part of the IKMC resource. As current estimates indicate that only a small percentage of genes are studied by the broad research community⁴⁶, the systematic approach to phenotyping and unrestricted access to data and mouse models provided by the IMPC promises to fill this large gap in our understanding of mammalian gene function.

Online Content Methods, along with any additional Extended Data display items and Source Data, are available in the online version of the paper; references unique to these sections appear only in the online paper.

Received 12 November 2015; accepted 10 August 2016.

Published online xx xx 2016.

- Cox, B. J. *et al.* Phenotypic annotation of the mouse X chromosome. *Genome Res.* **20**, 1154–1164 (2010).
- Justice, M. J. Capitalizing on large-scale mouse mutagenesis screens. *Nat. Rev. Genet.* **1**, 109–115 (2000).
- Kasarskis, A., Manova, K. & Anderson, K. V. A phenotype-based screen for embryonic lethal mutations in the mouse. *Proc. Natl Acad. Sci. USA* **95**, 7485–7490 (1998).
- Kile, B. T. & Hilton, D. J. The art and design of genetic screens: mouse. *Nat. Rev. Genet.* **6**, 557–567 (2005).
- Perrin, S. Preclinical research: Make mouse studies work. *Nature* **507**, 423–425 (2014).
- Prinz, F., Schlange, T. & Asadullah, K. Believe it or not: how much can we rely on published data on potential drug targets? *Nat. Rev. Drug Discov.* **10**, 712 (2011).
- Ayadi, A. *et al.* Mouse large-scale phenotyping initiatives: overview of the European mouse disease clinic (EUMODIC) and of the Wellcome Trust Sanger Institute mouse genetics project. *Mamm. Genome* **23**, 600–610 (2012).
- Bradley, A. *et al.* The mammalian gene function resource: the international knockout mouse consortium. *Mamm. Genome* **23**, 580–586 (2012).
- Hrabě de Angelis, M. *et al.* Analysis of mammalian gene function through broad-based phenotypic screens across a consortium of mouse clinics. *Nat. Genet.* **47**, 969–978 (2015).
- Skarnes, W. C. *et al.* A conditional knockout resource for the genome-wide study of mouse gene function. *Nature* **474**, 337–342 (2011).
- Valenzuela, D. M. *et al.* High-throughput engineering of the mouse genome coupled with high-resolution expression analysis. *Nat. Biotechnol.* **21**, 652–659 (2003).
- White, J. K. *et al.* Genome-wide generation and systematic phenotyping of knockout mice reveals new roles for many genes. *Cell* **154**, 452–464 (2013).

13. Adams, D. *et al.* Bloomsbury report on mouse embryo phenotyping: recommendations from the IMPC workshop on embryonic lethal screening. *Dis. Model. Mech.* **6**, 571–579 (2013).
14. Ashburner, M. *et al.* The Gene Ontology Consortium. Gene ontology: tool for the unification of biology. *Nat. Genet.* **25**, 25–29 (2000).
15. Blomen, V. A. *et al.* Gene essentiality and synthetic lethality in haploid human cells. *Science* **350**, 1092–1096 (2015).
16. Hart, T. *et al.* High-resolution CRISPR screens reveal fitness genes and genotype-specific cancer liabilities. *Cell* **163**, 1515–1526 (2015).
17. Wang, T. *et al.* Identification and characterization of essential genes in the human genome. *Science* **350**, 1096–1101 (2015).
18. Sharpe, J. *et al.* Optical projection tomography as a tool for 3D microscopy and gene expression studies. *Science* **296**, 541–545 (2002).
19. Wong, M. D., Dorr, A. E., Walls, J. R., Lerch, J. P. & Henkelman, R. M. A novel 3D mouse embryo atlas based on micro-CT. *Development* **139**, 3248–3256 (2012).
20. Wong, M. D., Maezawa, Y., Lerch, J. P. & Henkelman, R. M. Automated pipeline for anatomical phenotyping of mouse embryos using micro-CT. *Development* **141**, 2533–2541 (2014).
21. Wong, M. D. *et al.* 4D atlas of the mouse embryo for precise morphological staging. *Development* **142**, 3583–3591 (2015).
22. Weninger, W. J. *et al.* Phenotyping structural abnormalities in mouse embryos using high-resolution episcopic microscopy. *Dis. Model. Mech.* **7**, 1143–1152 (2014).
23. Liu, B. *et al.* Cbx4 regulates the proliferation of thymic epithelial cells and thymus function. *Development* **140**, 780–788 (2013).
24. Horvitz, H. R. & Sulston, J. E. Isolation and genetic characterization of cell-lineage mutants of the nematode *Caenorhabditis elegans*. *Genetics* **96**, 435–454 (1980).
25. Burga, A., Casanueva, M. O. & Lehner, B. Predicting mutation outcome from early stochastic variation in genetic interaction partners. *Nature* **480**, 250–253 (2011).
26. Raj, A., Rifkin, S. A., Andersen, E. & van Oudenaarden, A. Variability in gene expression underlies incomplete penetrance. *Nature* **463**, 913–918 (2010).
27. Matzuk, M. M., Kumar, T. R. & Bradley, A. Different phenotypes for mice deficient in either activins or activin receptor type II. *Nature* **374**, 356–360 (1995).
28. Song, J. *et al.* The type II activin receptors are essential for egg cylinder growth, gastrulation, and rostral head development in mice. *Dev. Biol.* **213**, 157–169 (1999).
29. Georgi, B., Voight, B. F. & Bućan, M. From mouse to human: evolutionary genomics analysis of human orthologs of essential genes. *PLoS Genet.* **9**, e1003484 (2013).
30. Dickerson, J. E., Zhu, A., Robertson, D. L. & Hentges, K. E. Defining the role of essential genes in human disease. *PLoS One* **6**, e27368 (2011).
31. Stenson, P. D. *et al.* Human Gene Mutation Database (HGMD): 2003 update. *Hum. Mutat.* **21**, 577–581 (2003).
32. Stenson, P. D. *et al.* The human gene mutation database: building a comprehensive mutation repository for clinical and molecular genetics, diagnostic testing and personalized genomic medicine. *Hum. Genet.* **133**, 1–9 (2014).
33. Welter, D. *et al.* The NHGRI GWAS catalog, a curated resource of SNP-trait associations. *Nucleic Acids Res.* **42**, D1001–D1006 (2014).
34. Schinzel, A. & Giedion, A. A syndrome of severe midface retraction, multiple skull anomalies, clubfeet, and cardiac and renal malformations in sibs. *Am. J. Med. Genet.* **1**, 361–375 (1978).
35. Piazza, R. *et al.* Recurrent SETBP1 mutations in atypical chronic myeloid leukemia. *Nat. Genet.* **45**, 18–24 (2013).
36. Moslemi, A. R. *et al.* Glycogenin-1 deficiency and inactivated priming of glycogen synthesis. *N. Engl. J. Med.* **362**, 1203–1210 (2010).
37. Malfatti, E. *et al.* A new muscle glycogen storage disease associated with glycogenin-1 deficiency. *Ann. Neurol.* **76**, 891–898 (2014).
38. Ballif, B. C. *et al.* Discovery of a previously unrecognized microdeletion syndrome of 16p11.2-p12.2. *Nat. Genet.* **39**, 1071–1073 (2007).
39. Lek, M. *et al.* Analysis of protein-coding genetic variation in 60,706 humans. *Nature* **536**, 285–291 (2016).
40. Petrovski, S., Wang, Q., Heinzen, E. L., Allen, A. S. & Goldstein, D. B. Genic intolerance to functional variation and the interpretation of personal genomes. *PLoS Genet.* **9**, e1003709 (2013).
41. Sulem, P. *et al.* Identification of a large set of rare complete human knockouts. *Nat. Genet.* **47**, 448–452 (2015).
42. MacArthur, D. G. *et al.* A systematic survey of loss-of-function variants in human protein-coding genes. *Science* **335**, 823–828 (2012).
43. Alkuraya, F. S. Human knockout research: new horizons and opportunities. *Trends Genet.* **31**, 108–115 (2015).
44. Narasimhan, V. M. *et al.* Health and population effects of rare gene knockouts in adult humans with related parents. *Science* **352**, 474–477 (2016).
45. Yang, H. *et al.* One-step generation of mice carrying reporter and conditional alleles by CRISPR/Cas-mediated genome engineering. *Cell* **154**, 1370–1379 (2013).
46. Edwards, A. M. *et al.* Too many roads not taken. *Nature* **470**, 163–165 (2011).

Supplementary Information is available in the online version of the paper.

Acknowledgements The authors thank all IMPC members and partners for their contribution to the consortium effort, including this study, and acknowledge the contributions of J. Rossant, S. L. Adamson, and T. Bubela. This work was supported by NIH grants U42 OD011185 (S.A.M.), U54 HG006332

(R.E.B., K.S.), U54 HG006348-S1 and OD011174 (A.L.B.), HG006364-03S1 and U42 OD011175 (K.C.K.L.), U54 HG006370 (P.F., A.-M.M., H.E.P., S.D.M.B.) and additional support provided by The Wellcome Trust, Medical Research Council Strategic Award (L.T., S.W., S.D.M.B.), Government of Canada through Genome Canada and Ontario Genomics (OGI-051)(C.M., S.D.M.B.), Wellcome Trust Strategic Award “Deciphering the Mechanisms of Developmental Disorders (DMDD)” (WT100160) (D.A., T.M.), National Centre for Scientific Research (CNRS), the French National Institute of Health and Medical Research (INSERM), the University of Strasbourg (UDS), the “Centre Européen de Recherche en Biologie et en Médecine”, the “Agence Nationale de la Recherche” under the frame programme “Investissements d’Avenir” labelled ANR-10-IDEX-0002-02, ANR-10-INBS-07 PHENOMIN to (Y.H.), The German Federal Ministry of Education and Research by Infrafrontier grant O1KX1012 (S.M., V.G.D., H.F., M.H.d.A.)

Author Contributions M.E.D., A.M.F., X.J., L.T., M.D.W., J.K.W., T.F.M., W.J.W., H.W., D.J.A., M.B., and S.A.M. contributed to the data analysis and writing of the paper. A.Y., A.B., L.B., L.B.C., F.C., B.D., H.F., A. Galli, A.G., V. G.-D., S.G., S.M., S.A.M., L.M.J.N., E.R., J.R.S., M.S., W.C.S., R.R.S., L.T., S.W. and J.K.W. generated animal models and identified lethal genes. M.E.D., A.M.F., X.J., H.W., L.T., J.M.B., N.R.H., T.F.M., M.E.Dolan and S.A.M. contributed to gene list analysis. H.A., L.B., L.B.C., C.N.B., J.C., J.M.D., M.E.D., S.M.E., A.M.F. A. Galli, C.-W.H., S.J.J., S.K., L.C.K., L.L., M.M., M.L.M., T.M., S.A.M., S.N., L.M.J.N., K.A.P., D.R., E.R., Z. S.-K., M.T., L.T., A.T., O.W., W.J.W., J.K.W. and L.W. contributed to the secondary lethal screen and data analysis. J.M.B., D.C., J.G., N.R.H., T.N.L., J.M., I.T. and J.W. provided informatics support. M.D.W. and R.M.H. performed the automated 3D analysis. J.M.B., N.R.H., I.T., J.W. and H.W. developed and implemented the IMPC portal, X.J., M.J.D., S.A.M., M.L., K.E.S., D.G.M., D.J.A. and M.B. contributed to the essential gene and human disease analysis. M.E.D., A.M.F., X.J., L.T., M.D.W., J.K.W., T.F.M., W.J.W., H.W., S.W., R.R.S., J.M.D., D.G.M., D.B.W., G.P.T.-V., X.G., P.F., W.C.S., A.B., M.J.J., H.E.P., M.Moore, S.W., R.E.B., K.S., M.H.d.A., Y.H., T.M., A.-M.M., R.M.H., S.D.M.B., D.J.A., K.C.K.L., C.M., A.L.B., M.B. and S.A.M. contributed to the design, management, execution of the work and review of the manuscript.

Author Information All data are freely available from the IMPC database hosted at EMBL-EBI via a web portal (mousephenotype.org), ftp (ftp://ftp.ebi.ac.uk/pub/databases/impc) and automatic programmatic interfaces. An archived version of the database will be maintained after cessation of funding (exp. 2021) for an additional 5 years. Allele and phenotype summaries are additionally archived with Mouse Genome Informatics at the Jackson Laboratory via direct data submissions (J:136110, J:148605, J:157064, J:157065, J:188991, J:211773). Reprints and permissions information is available at www.nature.com/reprints. The authors declare no competing financial interests. Readers are welcome to comment on the online version of the paper. Correspondence and requests for materials should be addressed to S.A.M. (steve.murray@jax.org).

Reviewer Information *Nature* thanks N. Copeland, L. Niswander and the other anonymous reviewer(s) for their contribution to the peer review of this work.

The International Mouse Phenotyping Consortium (Participants are arranged by institution.)

The Jackson Laboratory Matthew McKay¹, Barbara Urban¹, Caroline Lund¹, Erin Froeter¹, Taylor LaCasse¹, Adrienne Mehalow¹, Emily Gordon¹, Leah Rae Donahue¹, Robert Taft¹, Peter Kutney¹, Stephanie Dion¹, Leslie Goodwin¹, Susan Kales¹, Rachel Urban¹ & Kristina Palmer¹;
Infrastructure Nationale PHENOMIN, Institut Clinique de la Souris (ICS) Fabien Pertuy², Deborah Bitz², Bruno Weber², Patrice Goetz-Reiner², Hughes Jacobs², Elise Le Marchand², Amal El Amri², Leila El Fertak², Hamid Ennah², Dalila Ali-Hadjji², Abdel Ayadi², Marie Wattenhofer-Donze², Sylvie Jacquot², Philippe André², Marie-Christine Birling², Guillaume Pavlovic² & Tania Sorg²; **Charles River Laboratories** Iva Morse³ & Frank Benso³; **MRC Harwell** Michelle E. Stewart⁴, Carol Copley⁴, Jackie Harrison⁴ & Samantha Joynson⁴; **The Toronto Centre for Phenogenomics** Ruolin Guo⁵, Dawei Qu⁵, Shoshana Spring⁵, Lisa Yu⁵, Jacob Ellegood⁵, Lily Morikawa⁵, Xueyuan Shang⁵, Pat Feugas⁵, Amie Creighton⁵, Patricia Castellanos Penton⁵ & Ozge Danisman⁵; **The Wellcome Trust Sanger Institute** Nicola Genovese⁶, Catherine L. Tudor⁶, Angela L. Green⁶, Cecilia Icoresi Mazzeo⁶, Emma Siragher⁶, Charlotte Lillystone⁶, Elizabeth Tuck⁶, Diane Gleeson⁶, Debarati Sethi⁶, Tanya Bayzetyanova⁶, Jonathan Burvill⁶, Bishop Habib⁶, Lauren Weavers⁶, Ryea Maswood⁶, Evelina Miklejewski⁶, Michael Woods⁶, Evelyn Grau⁶, Stuart Newman⁶, Caroline Sinclair⁶ & Ellen Brown⁶; **RIKEN BioResource Center** Shinya Ayabe⁷, Mizuho Iwama⁷ & Ayumi Murakami⁷

¹The Jackson Laboratory, Bar Harbor, Maine 04609, USA.

²Infrastructure Nationale PHENOMIN, Institut Clinique de la Souris (ICS), et Institut de Génétique Biologie Moléculaire et Cellulaire (IGBMC) CNRS, INSERM, University of Strasbourg, Illkirch-Graffenstaden 67404, France.

³Charles River Laboratories, Wilmington, Massachusetts 01887, USA.

⁴Medical Research Council Harwell (Mammalian Genetics Unit and Mary Lyon Centre), Harwell, Oxfordshire OX11 0RD, UK.

⁵The Toronto Centre for Phenogenomics, Toronto, Ontario M5T 3H7, Canada.

⁶The Wellcome Trust Sanger Institute, Wellcome Trust Genome Campus, Hinxton, Cambridge CB10 1SA, UK.

⁷RIKEN BioResource Center, Tsukuba, Ibaraki 305-0074, Japan.

METHODS

Standardized, consortium-wide protocols are available at the IMPC portal (www.mousphenotype.org/impress). These procedures define the minimum standards, metadata and protocols for all publically available data. All mouse experiments were conducted in accordance with the governmental and funding regulations of the different member centres. Details of individual centre-specific methods are posted with the IMPRESS procedures. Additional details are provided below.

For all experiments, the sex of the embryos was determined and documented, but was not used as a covariate in the analyses. The investigators were blinded to genotype and sex in the evaluation of gross morphological phenotypes, but not for evaluation of 3D imaging datasets. For detection of lethality, at 0 out of 28 homozygous pups, using a binomial distribution ($\text{BINOMDIST}(0,28,0.25,1)$), $p = 0.000317479$. For automated 3D analysis a power analysis was reported previously⁵³. For gross morphology and manual annotation of micro-CT images, no statistical methods were used to predetermine sample size.

Mice. All mouse lines in this study are derived from IKMC ES cell resources. All mice are produced and maintained on a C57BL/6N genetic background, with support mice derived from C57BL/6NJ, C57BL/6NTac or C57BL/6Ncr1. Husbandry details vary by centre, and can be found at <http://www.mousephenotype.org/impress>. For timed matings, successful mating and fertilization (0h) was calculated to be the midpoint of the dark cycle before the appearance of the copulation plug.

Gene list analysis. Gene lists were filtered and analysed using MouseMine at MGI (www.mousemine.org). For segmentation of novel and prior reported knockout lines, alleles were filtered to include 'targeted' and 'null' mutations only, as these are comparable to the IKMC alleles in this study. A further filtering step was performed to include only lines for which phenotypic data (normal or abnormal) are reported.

GOSlim enrichment. Gene lists were analysed using the GOSlim tool hosted at Mouse Genome Informatics: http://www.informatics.jax.org/gotools/MGI_GO_Slim_Chart.html. Both experimental and computational analysis codes were included in the search.

Dissection and preparation of E9.5 and E15.5 embryos for OPT and micro-CT Imaging. Embryos were dissected in 37 °C phosphate buffered saline (PBS) (without $\text{Ca}^{2+}/\text{Mg}^{2+}$) containing heparin (1 unit/1 ml PBS). Extra-embryonic membranes were removed and the yolk sac collected for genotyping. The embryos were exsanguinated by severing the umbilical vessels with small scissors and rocking them in warm PBS/heparin for a maximum of 5 min for E9.5 embryos and 15 min for E15.5 embryos. Embryos were washed twice with PBS and immersion fixed in 20–40 × the volume of 4% paraformaldehyde (PFA) prepared in PBS. E9.5 embryos were fixed for 4 h at 4 °C or 2 h at room temperature (RT) and E15.5 embryos were fixed overnight at 4 °C. After fixation embryos were stored at 4 °C in PBS containing 0.02% sodium azide (0.2 g l^{-1} PBS).

Optical projection tomography. Sample preparation. Each E9.5 embryo was embedded in low-melting point agarose. The agarose plug was then subjected to a dehydration series using methanol (25%, 50%, 75%, 100% × 2) where the methanol solutions were replaced once per day. The agarose plug was then cleared with BABB (1:2 benzyl alcohol/benzyl peroxide) for three days. The BABB solution was replaced once per day during the clearing process.

Imaging. optical projection imaging was done as previously described⁴⁸. Briefly, each sample was excited by ultraviolet light filtered by the following excitation filter: Semrock 425/30 BrightLine Bandpass Filter, 25 mm [FF01-425/30-25]. Autofluorescence was captured by a CCD camera, where the emission was filtered using the following emission filter: 473 RazorEdge Long-pass Filter, U-grade, 50.8 mm [LP02-473RU-50.8-D]. The sample was rotated 360° at 0.3° increments, resulting in 1200 projections. The exposure time varied per image, but the average was 500 ms. The resultant 3D image file had an isotropic voxel size of $4.45 \mu\text{m}^3$.

Micro-computed tomography. Sample preparation. Each E15.5 embryo was subjected to hydrogel stabilization⁴⁹. Briefly, the embryo was incubated in 20 ml hydrogel solution containing a mixture of ice-cold 4% (wt) PFA, 4% (wt/vol) acrylamide (Bio-Rad), 0.05% (wt/vol) bis-acrylamide (Bio-Rad), 0.25% VA044 Initiator (Wako Chemicals USA), 0.05% (wt/vol) saponin (Sigma-Aldrich) and PBS at 4 °C for 3 days. After incubation, the tube containing the embryo was placed in a desiccation chamber where air in the tube was replaced with nitrogen gas. The tube was placed in a 37 °C water bath for 3 h. Lastly, the samples were separated from the encasing gel and placed into iodine solution. Each E15.5 mouse embryo was stained with 50 ml of 0.1 M iodine solution (Sigma-Aldrich) for 24 h. The iodine-stained embryo was then embedded in agarose in an 11-mm centrifuge tube and positioned in the micro-CT scanner for imaging.

Imaging. 3D data sets were acquired for each mouse embryo using a Skyscan 1172 high-resolution micro-CT scanner (Bruker). Each specimen was rotated 360°

around the vertical axis, generating 1200 views in 5 h, with the X-ray source set to 100 kVp and 100 μA and using a 0.5-mm aluminium filter. These image projections were reconstructed into digital cross-sections using the Feldkamp algorithm⁵⁰ for cone beam CT. The resulting 3D data block contained $2,000 \times 1,000 \times 1,000$ voxels of $13.4 \mu\text{m}^3$ voxel size.

High-resolution episcopic microscopy (HREM). Protocols for the preparation and imaging of embryos by HREM are described in detail in ref. 51. All analysis was performed on E14.5 embryos.

Automated image analysis. The automated image analysis was performed as fully described in ref. 52. The segmented 3D atlas of structures used to automate volume measurements was described and presented in ref. 53.

Dissection and preparation of P7 brains for whole brain MRI. Pups were tattooed and genotyped at P3 to determine homozygous viability. At P7, homozygous pups were sedated by intraperitoneal injection of ketamine (150 mg/kg) and xylazine (10 mg/kg) at 0.1 ml/10 g body weight. Pups were then transcardially flushed with 30 ml of PBS (Wisent) containing 1 unit/ml heparin and 2 mM Gadolinium (Gd) ('ProHance' gadoteridol, Bracco Diagnostics), followed by fixation with 30 ml of PBS containing 4% paraformaldehyde (PFA) (Electron Microscopy Sciences) and 2 mM Gd. Flushing and fixation proceeded at a slow flow rate of 1.0 ml min^{-1} at RT. Following perfusion, the brain was extracted with the skull, but with the skin, zygomatic bones, eyes, and lower jaw removed. The brain and remaining skull structure were incubated in 35 ml of 4% PFA containing 2 mM Gd overnight at 4 °C and then transferred to PBS containing 0.02% sodium azide with 2 mM Gd for at least 3 days before imaging.

Image acquisition. Images were acquired on a 7 Tesla MRI scanner (Varian Inc.)⁵⁴. The contrast required for registration and assessment of volume is not acceptable with our typical T2-weighted imaging sequence. Therefore, diffusion-weighted imaging was performed to enhance the contrast between white and grey matter to aid in the registration and volume measurements.

Diffusion imaging sequence. The diffusion sequence uses an in-house custom built 16-coil solenoid array to acquire images from 16 brains in parallel⁵⁵. The diffusion sequence used was a 3D diffusion-weighted FSE, with $\text{TR} = 270 \text{ ms}$, echo train length = 6, first $\text{TE} = 30 \text{ ms}$, $\text{TE} = 10 \text{ ms}$ for the remaining 5 echoes, one average, $\text{FOV} = 25 \text{ mm} \times 14 \text{ mm} \times 14 \text{ mm}$, and a matrix size of $450 \times 250 \times 250$, which yielded an image with $56 \mu\text{m}$ isotropic voxels. One $b = 0 \text{ s mm}^{-2}$ image was acquired and 6 high b -value ($b = 2147 \text{ s mm}^{-2}$) images were acquired at the following directions (1,1,0), (1,0,1), (0,1,1), (−1,1,0), (−1,0,1) and (0,1,−1) corresponding to (G_x, G_y, G_z). Total imaging time was approximately 14 h.

Registration and analysis. To visualize and compare the mouse brains for the anatomical volume assessment the six high b -value images were averaged together to make a high contrast image necessary for accurate registration. Then these images were linearly (6 parameter followed by a 12 parameter) and nonlinearly registered together. All scans were then resampled with the appropriate transform and averaged to create a population atlas representing the average anatomy of the study sample. All registrations were performed using a combination of the *mni_autoreg* tools⁵⁶ and ANTS⁵⁷. The result of the registration was to have all scans deformed into exact alignment with each other in an unbiased fashion. For the volume measurements, this allowed the analysis of the deformations needed to take the anatomy of each individual mouse into this final atlas space, the goal being to model how the deformation fields relate to genotype^{54,58}. The Jacobian determinants of the deformation fields are then calculated as measures of volume at each voxel. These measurements were examined on a voxel-wise basis in order to localize the differences found within regions or across the brain. Multiple comparisons were controlled for by using the false discovery rate (FDR)⁵⁹.

LacZ staining. Whole litters of E12.5 embryos were fixed in 4% PFA for 1 h in PBS at 4 °C with gentle shaking. Embryos were subsequently washed 3 × in detergent rinse (2 mM MgCl_2 , 0.02% igepal, 0.01% sodium deoxycholate and 0.1 M phosphate ($\text{K}_2\text{HPO}_4/\text{KH}_2\text{PO}_4$) buffer, pH 7.5) at 4 °C, and moved to X-gal staining solution (2 mM MgCl_2 , 0.02% igepal, 0.01% sodium deoxycholate, 5 mM potassium ferricyanide, 1 mg ml^{-1} X-gal in 0.1 M phosphate buffer, pH 7.5) for 48 h at 4 °C with gentle shaking in the dark. Stained embryos were rinsed briefly in PBS at RT, then post-fixed overnight at 4 °C in 4% PFA. After three rinses in PBS, embryos were transferred to a 50% glycerol/PBS solution for imaging and storage. Images were taken using centre-specific equipment, using standard orientations. Portions of the tail of individual stained embryos were removed for genotyping after imaging and assayed for zygosity and sex.

Identification of human orthologues of essential genes and non-lethal genes. To investigate the relevance of novel developmental phenotypes uncovered in the IMPC project, we combined the IMPC data with phenotype data for targeted loss-of-function mutant lines reported in the MGI⁶⁰. Genes annotated with any of 50 mouse phenotype terms including prenatal, perinatal and postnatal lethal phenotypes⁶¹ (Supplementary Table 7) were considered to be essential genes

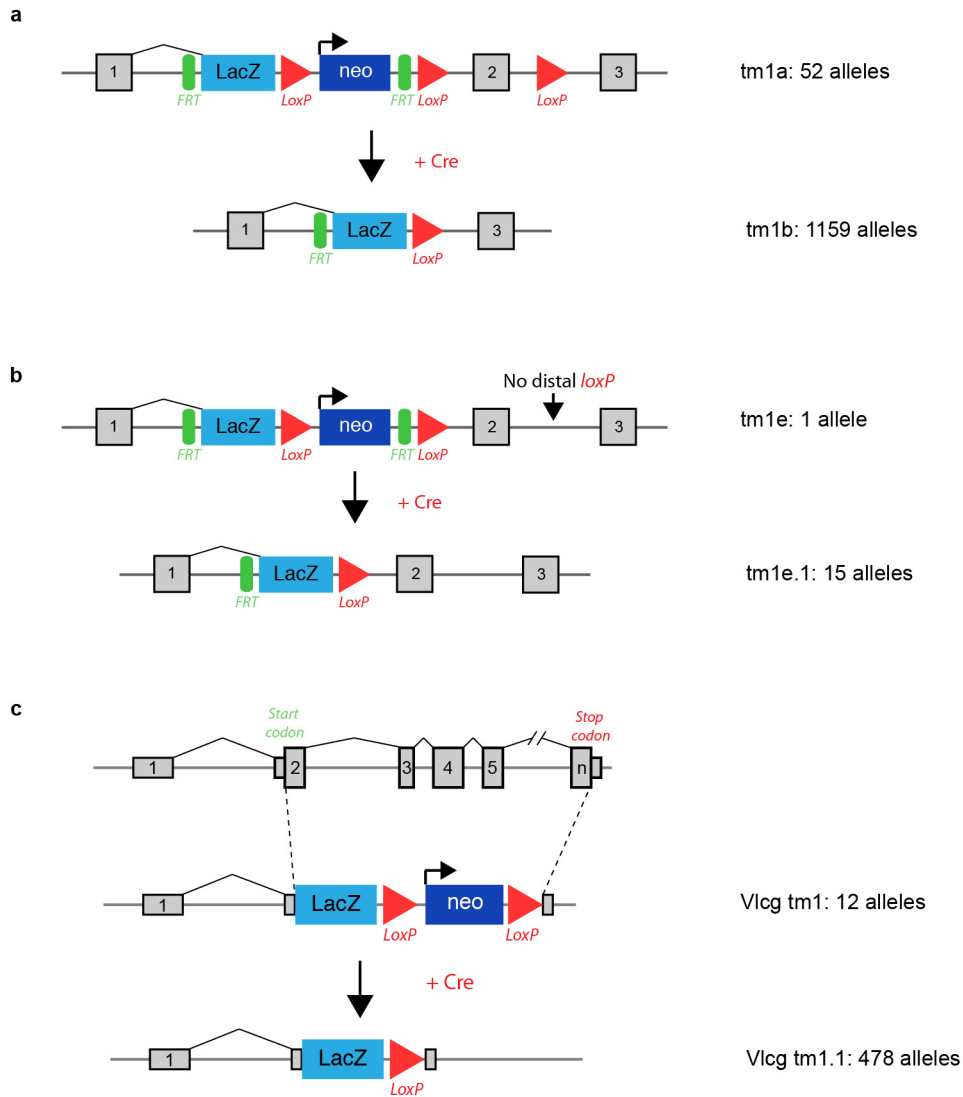
($n = 3,023$) (Supplementary Table 8). The MGI database was also used to select genes with reported targeted loss-of-function phenotypes that were not embryo or pre-weaning lethal (non-essential genes; $n = 4,995$). The IMPC effort expanded these lists with 252 essential genes, 101 genes with sub-viable phenotypes and 701 genes with viable mutant phenotypes. Whenever discrepancy appeared between the lethality status reported in publications (that is, in MGI) and in the IMPC data, we included phenotypes reported by IMPC, as these lines were generated on a defined C57BL/6N background and phenotyped using a standardized pipeline. We used the MGI mouse-human orthology annotation resulting in 3,229 essential and 4,757 non-essential human orthologues with unambiguous chromosomal position. Annotations of all human protein-coding genes (Ensembl Genes version 82, ref. 62), including essential/non-essential status, RVIS (ref. 63), pLI scores (Exome Aggregation Consortium) and human disease annotations from HGMD (ref. 64) and OMIM (ref. 65), are listed in Supplementary Table 8. Enrichment of HGMD disease genes between our gene sets of interest (that is, EGs, NEGs and all protein-coding genes) was assessed by two-sided Fisher's exact test. EG versus NEG (odds ratio = 2.00, $P = 7.80 \times 10^{-46}$), EG versus All (odds ratio = 3.13, $P = 2.42 \times 10^{-160}$), NEG versus All (odds ratio = 1.56, $P = 1.83 \times 10^{-29}$). Difference in intolerance scores between our gene sets of interest was assessed by one-sided Wilcoxon rank-sum test. RVIS: EG versus NEG ($P < 2.2 \times 10^{-16}$), EG versus All ($P < 2.2 \times 10^{-16}$), NEG versus All ($P = 0.579$). pLI: EG versus NEG ($P < 2.2 \times 10^{-16}$), EG versus All ($P < 2.2 \times 10^{-16}$), All versus NEG ($P = 4.15 \times 10^{-05}$).

Overlap between cell-essential genes in human haploid cells and human orthologues of essential genes in the mouse. We used data from three recent publications on genome-wide screens for cell-essential genes in human cells to address the overlap between essential genes in the human and mouse genome^{66–68}. From these papers, we selected 1,580 core EGs (genes above essentiality threshold in at least 3 out of 5 cell lines in the study) from Hart *et al.*, 1,739 core EGs (genes above essentiality threshold in at least 2 out of 4 cell lines in the study) from Wang *et al.* and 1,734 core EGs (genes above essentiality threshold in at least 1 out of 2 cell lines in the study) from Blomen *et al.* We used the combined IMPC-MGI EG list ($n = 3,326$, see above) to assess the overlap between human cell-essential genes identified in these three studies and essential genes in the mouse.

Identification of genes encompassing or surrounding disease- and trait-associated SNPs ('GWAS hits'). 6,384 protein-coding genes encompassing and/or neighbouring disease- or trait-associated variants ('GWAS genes') were obtained from the GWAS Catalog⁶⁹ (downloaded on April 29, 2016). Specifically, we used the 'mapped genes' from the GWAS Catalog which are defined as genes mapped to the strongest SNP from GWAS reports. The mapped genes are defined as the genes encompassing the GWAS SNP(s), (that is, located in coding or intragenic regions; $n = 4,228$) or the two genes that map upstream and downstream of the GWAS SNP(s) (that is, in intergenic regions; $n = 3,422$). Enrichment of GWAS genes between our gene sets of interest was assessed by two-sided Fisher's exact test. P values in Fisher's exact test for enrichment of genes surrounding GWAS hits between: EG versus NEG (odds ratio = 1.16, $P = 0.0015$), EG versus All (odds ratio = 1.56, $P = 5.80 \times 10^{-31}$), NEG versus All (odds ratio = 1.35, $P = 1.18 \times 10^{-19}$).

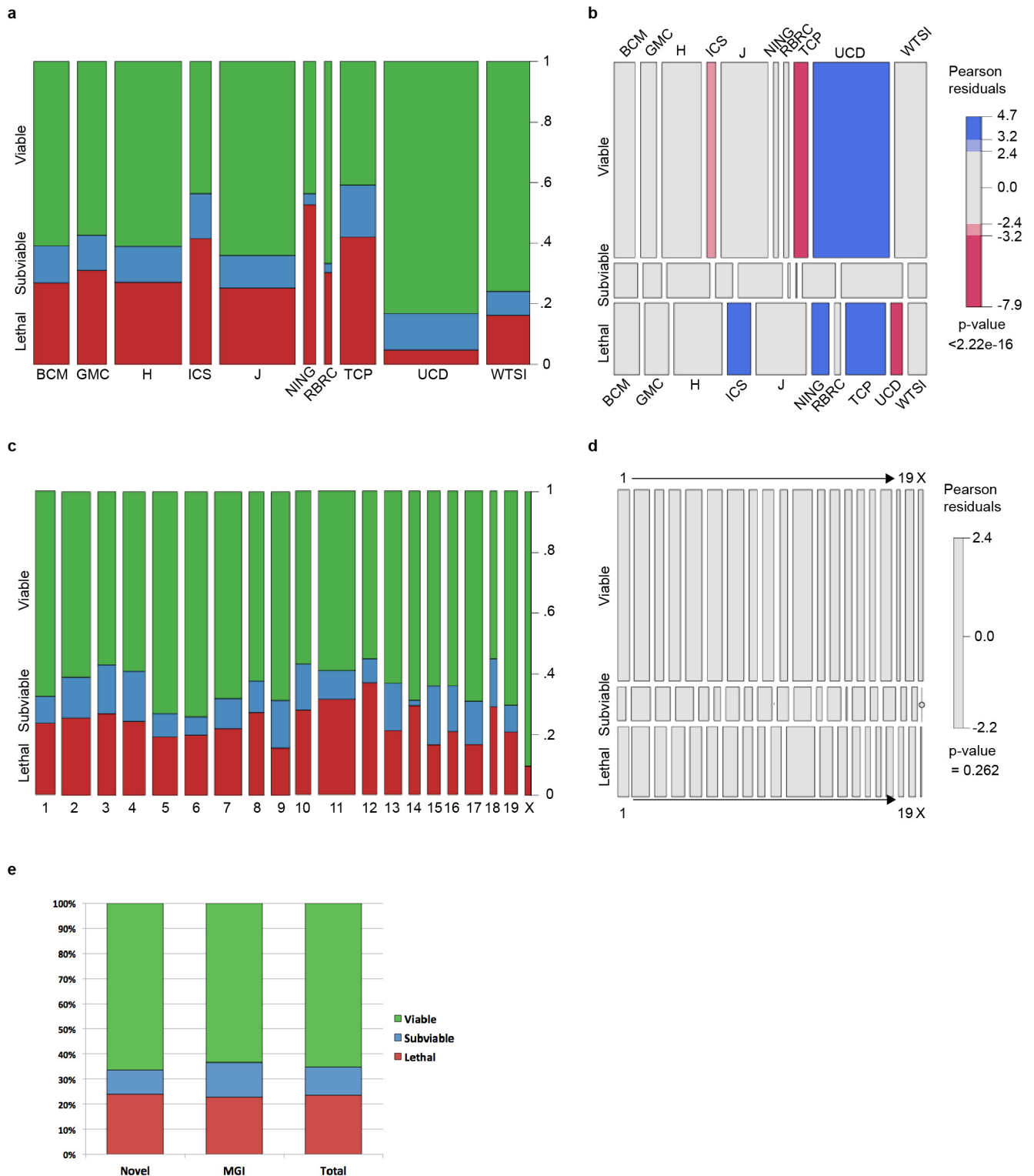
Code accessibility. Analysis code for bioinformatics data presented in Figs 1 and 5 can be accessed at <https://github.com/IMPC2015/code>.

48. Wong, M. D., Dazai, J., Walls, J. R., Gale, N. W. & Henkelman, R. M. Design and implementation of a custom built optical projection tomography system. *PLoS One* **8**, e73491 (2013).
49. Wong, M. D., Spring, S. & Henkelman, R. M. Structural stabilization of tissue for embryo phenotyping using micro-CT with iodine staining. *PLoS One* **8**, e84321 (2013).
50. Feldkamp, L. & Davis, L. Practical cone-beam tomography. *J. Opt. Soc. Am. A* (1984).
51. Weninger, W. J. *et al.* Phenotyping structural abnormalities in mouse embryos using high-resolution episcopic microscopy. *Dis. Model. Mech.* **7**, 1143–1152 (2014).
52. Wong, M. D., Maezawa, Y., Lerch, J. P. & Henkelman, R. M. Automated pipeline for anatomical phenotyping of mouse embryos using micro-CT. *Development* **141**, 2533–2541 (2014).
53. Wong, M. D., Dorr, A. E., Walls, J. R., Lerch, J. P. & Henkelman, R. M. A novel 3D mouse embryo atlas based on micro-CT. *Development* **139**, 3248–3256 (2012).
54. Nieman, B. J., Flenniken, A. M., Adamson, S. L., Henkelman, R. M. & Sled, J. G. Anatomical phenotyping in the brain and skull of a mutant mouse by magnetic resonance imaging and computed tomography. *Physiol. Genomics* **24**, 154–162 (2006).
55. Nieman, B. J. *et al.* Mouse behavioral mutants have neuroimaging abnormalities. *Hum. Brain Mapp.* **28**, 567–575 (2007).
56. Collins, D. L., Neelin, P., Peters, T. M. & Evans, A. C. Automatic 3D intersubject registration of MR volumetric data in standardized Talairach space. *J. Comput. Assist. Tomogr.* **18**, 192–205 (1994).
57. Avants, B. B. *et al.* A reproducible evaluation of ANTs similarity metric performance in brain image registration. *Neuroimage* **54**, 2033–2044 (2011).
58. Lau, J. C. *et al.* Longitudinal neuroanatomical changes determined by deformation-based morphometry in a mouse model of Alzheimer's disease. *Neuroimage* **42**, 19–27 (2008).
59. Genovese, C. R., Lazar, N. A. & Nichols, T. Thresholding of statistical maps in functional neuroimaging using the false discovery rate. *Neuroimage* **15**, 870–878 (2002).
60. Eppig, J. T., Blake, J. A., Bult, C. J., Kadin, J. A. & Richardson, J. E. The Mouse Genome Database (MGD): facilitating mouse as a model for human biology and disease. *Nucleic Acids Res.* **43**, D726–D736 (2015).
61. Smith, C. L. & Eppig, J. T. Expanding the mammalian phenotype ontology to support automated exchange of high throughput mouse phenotyping data generated by large-scale mouse knockout screens. *J. Biomed. Semantics* **6**, 11 (2015).
62. Cunningham, F. *et al.* Ensembl 2015. *Nucleic Acids Res.* **43**, D662–D669 (2015).
63. Petrovski, S., Wang, Q., Heinzen, E. L., Allen, A. S. & Goldstein, D. B. Genic intolerance to functional variation and the interpretation of personal genomes. *PLoS Genet.* **9**, e1003709 (2013).
64. Stenson, P. D. *et al.* Human Gene Mutation Database (HGMD): 2003 update. *Hum. Mutat.* **21**, 577–581 (2003).
65. Hamosh, A., Scott, A. F., Amberger, J. S., Bocchini, C. A. & McKusick, V. A. Online Mendelian Inheritance in Man (OMIM), a knowledgebase of human genes and genetic disorders. *Nucleic Acids Res.* **33**, D514–D517 (2005).
66. Hart, T. *et al.* High-Resolution CRISPR Screens Reveal Fitness Genes and Genotype-Specific Cancer Liabilities. *Cell* **163**, 1515–1526 (2015).
67. Wang, T. *et al.* Identification and characterization of essential genes in the human genome. *Science* **350**, 1096–1101 (2015).
68. Blomen, V. A. *et al.* Gene essentiality and synthetic lethality in haploid human cells. *Science* **350**, 1092–1096 (2015).
69. Welter, D. *et al.* The NHGRI GWAS Catalog, a curated resource of SNP-trait associations. *Nucleic Acids Res.* **42**, D1001–D1006 (2014).



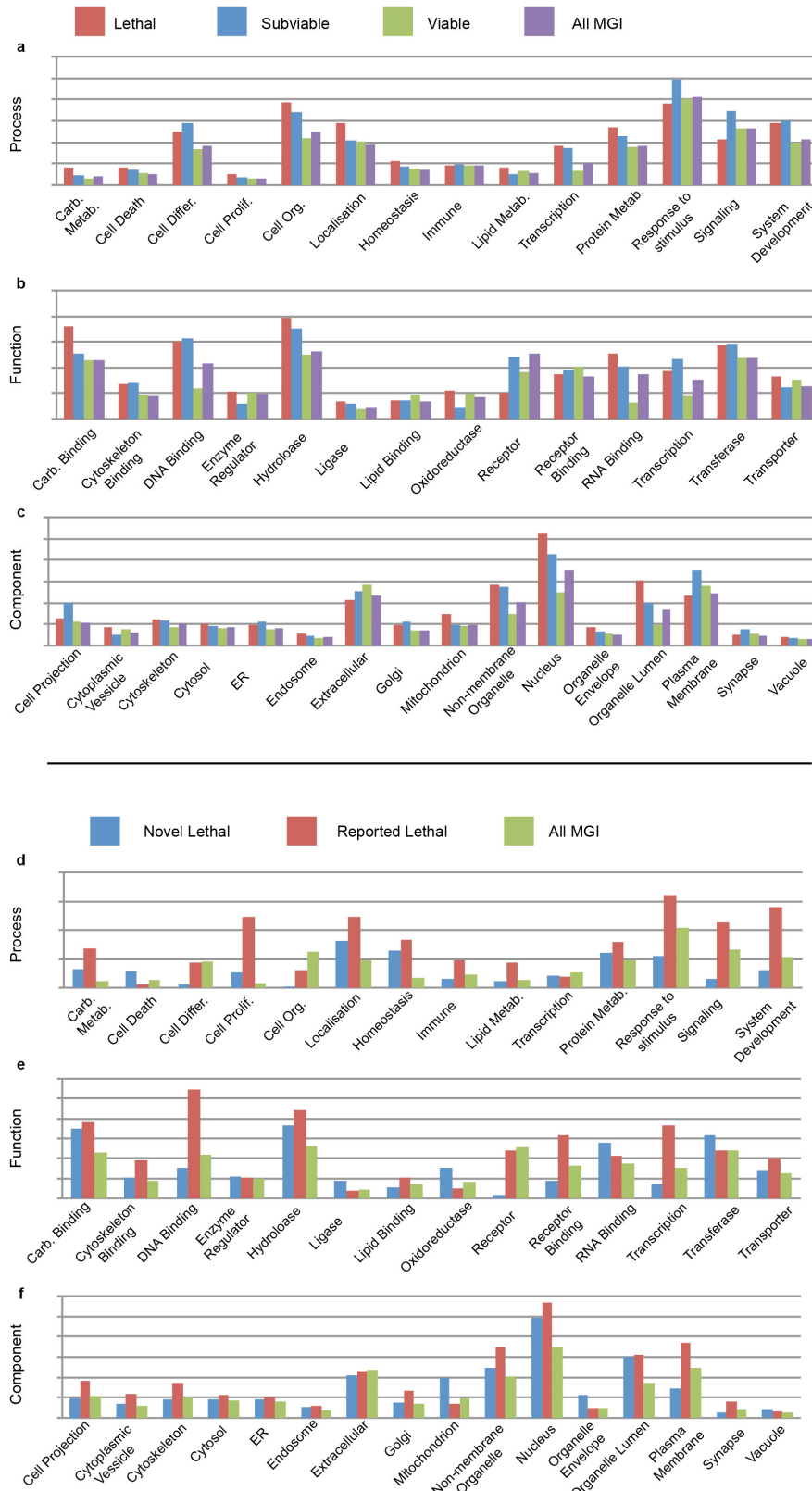
Extended Data Figure 1 | Standard IMPC allele variants included in this study. **a**, Conditional-ready, knockout-first allele (tm1a) design (top) with LacZ reporter, and the Cre-converted (tm1b, bottom) version lacking the neo cassette and critical exon. The promoter driven variant is illustrated. **b**, Schematic of the small number of alleles included where the distal loxP had been lost during targeting (tm1e, top) and the converted (tm1e.1)

variant with the neo cassette removed. **c**, Velocigene 'definitive null' design (top, tm1) where the LacZ cassette replaces the coding sequence of the target gene, and Cre-excised variant (bottom, tm1.1). Details of all alleles used are listed in Supplementary Table 2 and 5. Additional details and schematics of all allele variants are available at <http://www.mousephenotype.org/about-ikmc/targeting-strategies>.



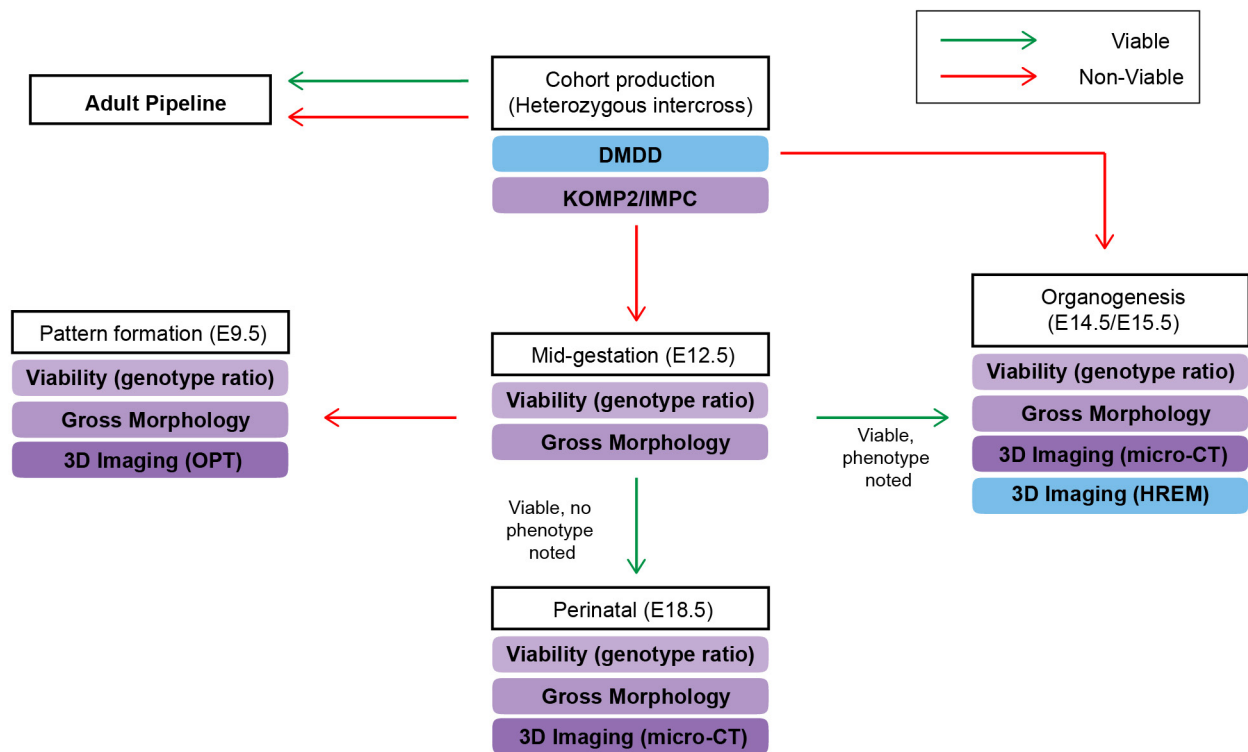
Extended Data Figure 2 | Distribution of lethal, subviable and viable lines for each IMPC Centre. Spine (a) and mosaic (b) plots of progress examining primary viability of IMPC lines for each IMPC Centre, segmented by 'Lethal', 'Subviable' or 'Viable' outcome. The mosaic plot shows the significant overrepresentation of viable lines from UCD and lethal lines from ICS, NING, and TCP. c, d, Spine and mosaic plots of primary viability outcome by chromosome, showing no significant deviation from the expected distribution. e, Comparison of the percentage

of viable, subviable, and lethal lines between genes for which no targeted knockout alleles have been reported (novel) and genes for which one or more knockout alleles has been reported. BCM, Baylor College of Medicine; GMC, German Mouse Clinic; H, MRC Harwell; ICS, Institut Clinique del la Souris (PHENOMIN); J, The Jackson Laboratory; NING, Model Animal Research Center, Nanjing University; RBRC, RIKEN BioResource Center; TCP, Toronto Centre for Phenogenomics; UCD, University of California, Davis; WTSI, Wellcome Trust Sanger Institute.



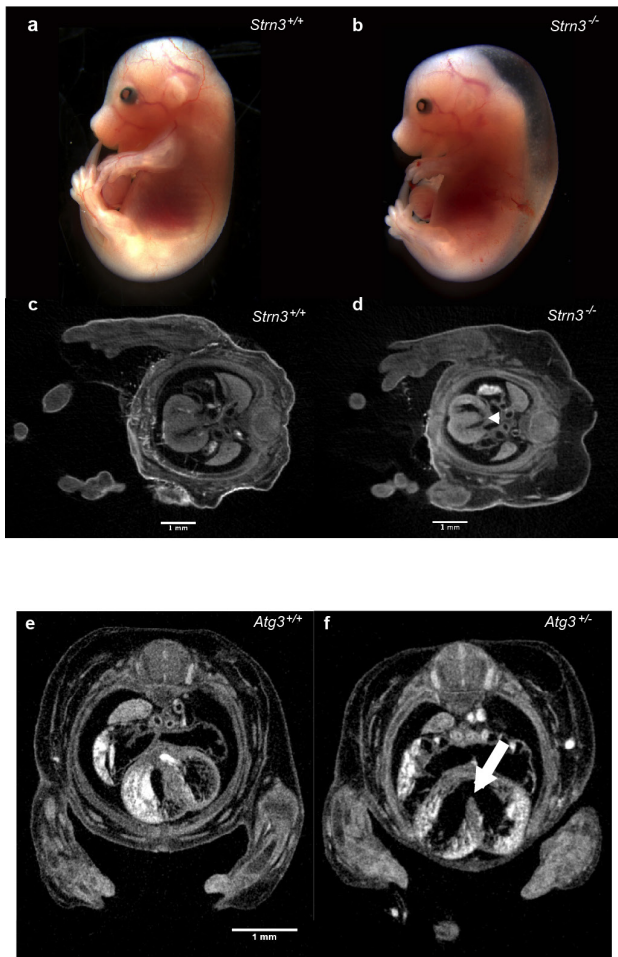
Extended Data Figure 3 | Multiple GOSlim categories show enrichment for lethal and subviable genes versus viable genes from the IMPC data set. The analysis was performed for GO Process (a), GO Function (b) and GO Component (c) categories. On the x axis is the proportion of genes in

each class that are annotated for the GO Slim group for each category. d-f, Novel lethal IMPC genes, previously reported IMPC genes and all MGI genes were subject to the same analysis, showing the large effect analysis and characterization of lethal genes has on GO analysis.

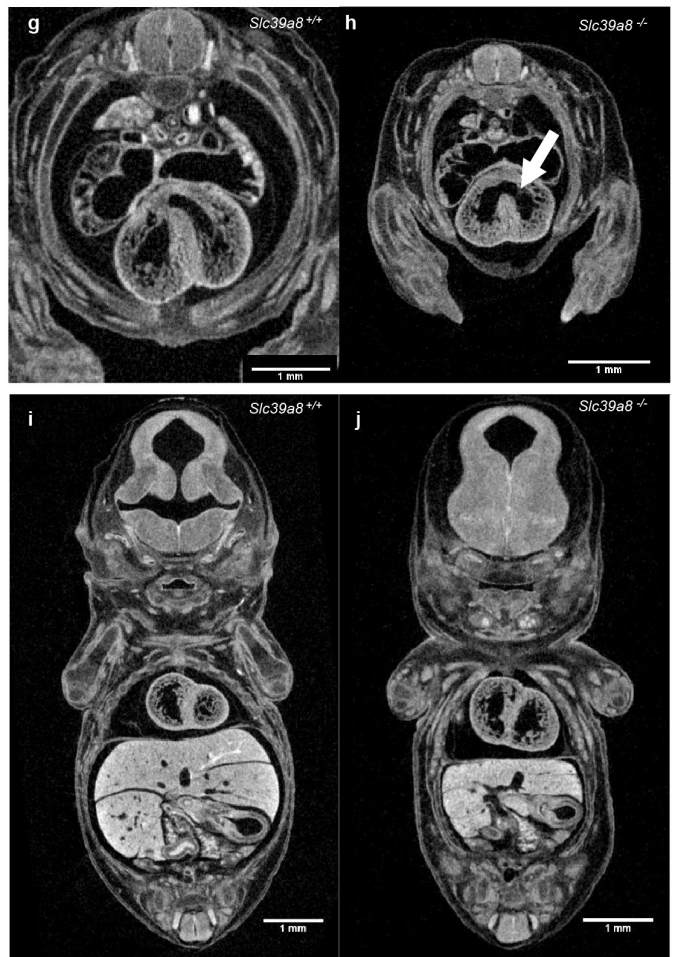


Extended Data Figure 4 | Schematic of the IMPC embryonic lethal phenotyping pipeline. Lines were defined as lethal if zero homozygous animals were identified after 28+ animals had been genotyped. The KOMP2/IMPC centres began with a mid-gestation (E12.5) screen, while the DMDD program initiated screening at the organogenesis phase (E14.5). If no homozygotes were identified (after ≥ 28 embryos screened), centres examined and characterized embryos at the pattern formation stage (E9.5). Homozygous embryos at this stage were scored for gross anatomical defects and imaged using OPT. If live homozygotes were

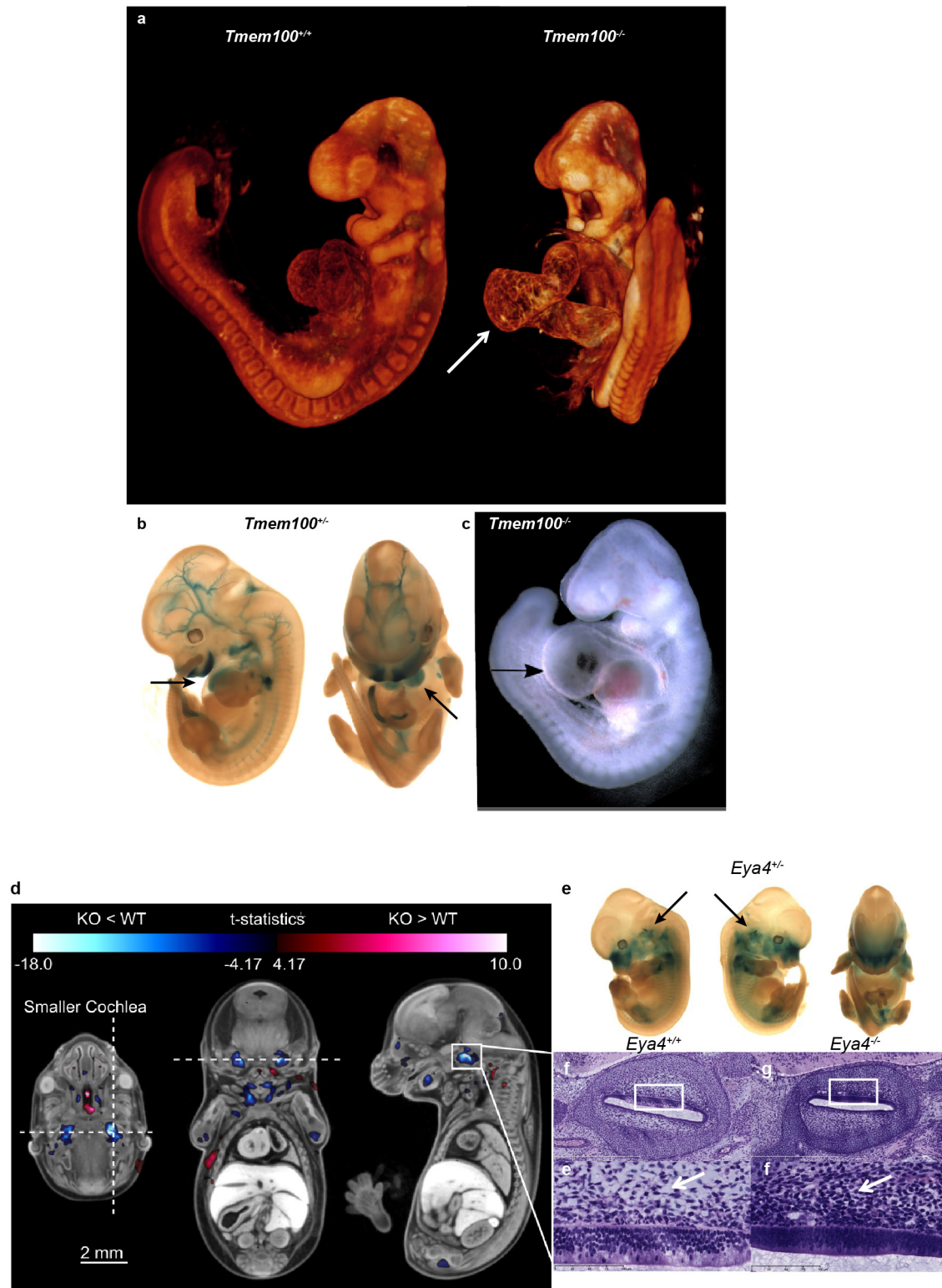
identified at E12.5, centres proceeded with the screen at E15.5 or E18.5. This decision was based on the presence of any observable phenotype at E12.5 and was at the discretion of the centre. Embryos collected at E15.5 were imaged via iodine-contrast microCT. Once sufficient numbers were collected, image registration and quantitative volumetric analysis was performed. Each time point should be considered independently, as some included strains have not been completely analysed and progression through each time point is at the discretion of the centre. For each term, two mutants with the same phenotype were required to score a hit.



Extended Data Figure 5 | Cardiac defects in *Strn3*, *Atg3*, and *Slc39a8* mutant embryos. **a, b,** Severe fetal oedema and sporadic haemorrhaging in E15.5 homozygous mutant embryos versus controls ($n = 7$ mutants analysed) **c, d,** Subtle but consistent cardiac septal defects (arrowhead) observed in transverse micro-CT volume sections in *Strn3*^{-/-} embryos (**d**) versus control (**c**) ($n = 5$ mutants analysed). **e, f,** *Atg3*^{+/-} (**e**) and *Atg3*^{-/-} (**f**) E14.5 embryos imaged by micro-CT after contrast staining showed evidence of heart morphological defects including ventricular septal



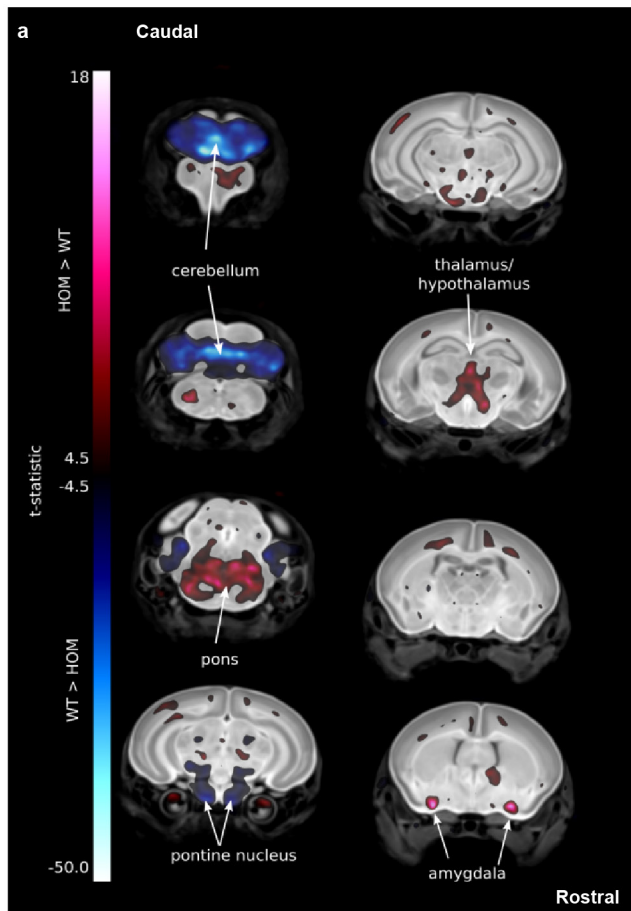
defects (white arrows in **f**). *Atg3*^{-/-} mice also showed abnormal atrio-ventricular valves ($n = 4$ mutants analysed). **g-j,** Transverse (**g, h**) and coronal (**i, j**) sections through micro-CT volumes of mutant and control *Slc39a8* E14.5 embryos revealed heart morphological defects including ventricular septal defects (white arrows in **h**). *Slc39a8*^{-/-} mice also showed the absence of sternum, a small chest cavity and a small liver (**j**) ($n = 4$ mutants analysed).



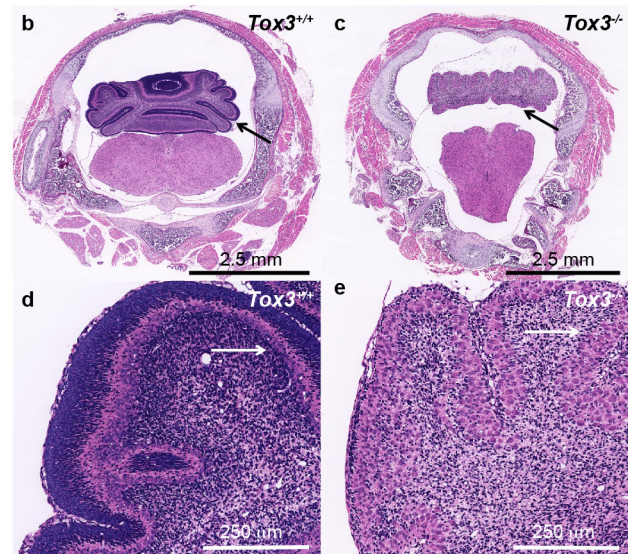
Extended Data Figure 6 | See next page for caption.

Extended Data Figure 6 | High-resolution 3D imaging reveals phenotypes in *Tmem100* and *Eya4* mutant embryos. *Tmem100*^{-/-} embryos had abnormal heart development compared to *Tmem100*^{+/+} controls. E9.5 *Tmem100*^{-/-} embryos had large pericardial effusion and cardiac dysmorphology and enlargement (arrow) when compared to E9.5 *Tmem100*^{+/+} (wild-type) embryos as seen by OPT imaging (a) and bright-field microscopy (c) resulting in lethality. (*n* = 8 *Tmem100*^{+/+} versus *n* = 8 *Tmem100*^{-/-}, with all 8 showing the defect). **b**, LacZ expression in the E12.5 *Tmem100*^{+/-} embryo indicated expression in the heart (arrows), blood vessels and craniofacial regions (blue). **d–i**, MicroCT imaging revealed a small cochlear volume in E15.5 *Eya4*^{-/-} embryos. E15.5 *Eya4*^{-/-} embryos were registered to an average control data set of the same age followed by automated analysis to show that mutant embryos had a statistically smaller cochlear volume compared to *Eya4*^{+/+} (wild-type) embryos. **d**, Transverse, coronal, and sagittal sections through the right cochlea are marked with a horizontal and vertical dashed line in

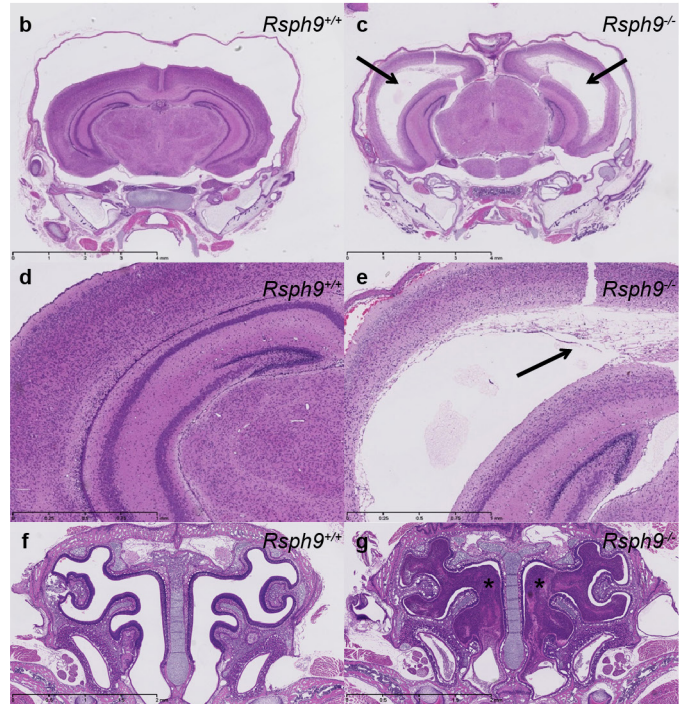
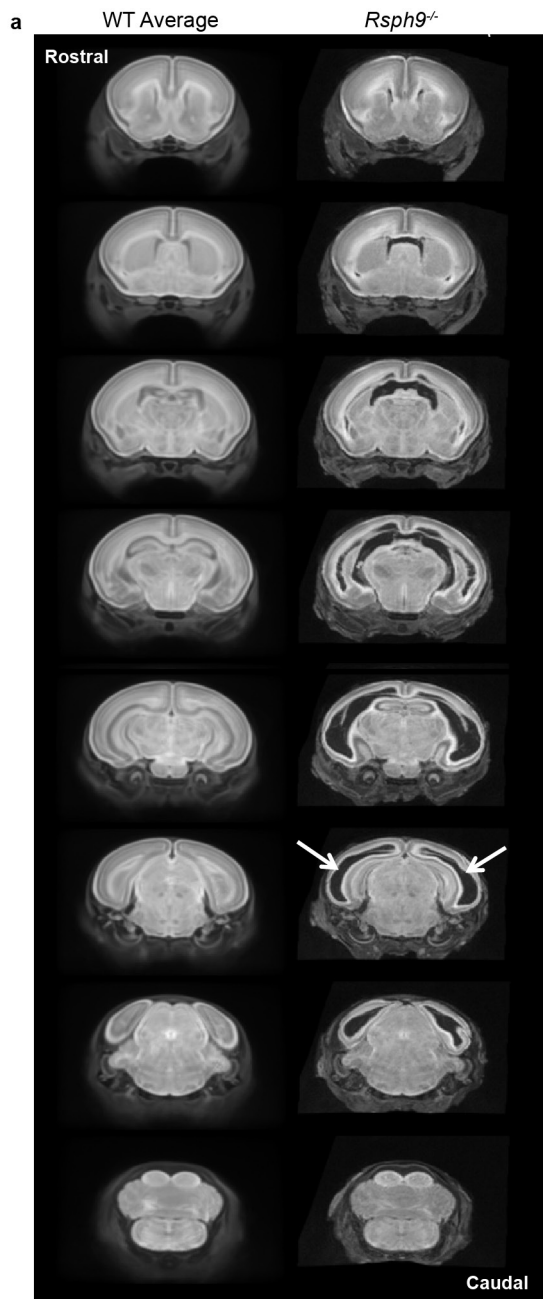
the transverse section to indicate the location of the coronal and sagittal sections, respectively. The colours correspond to areas of larger (red) and smaller (blue) volumes in the knockout embryos. The colour bar minimum corresponds to a false discovery rate (FDR) threshold of 5%. Hypoplastic bilateral cochlear structures are highlighted in blue, (*n* = 8 *Eya4*^{+/+} (wild-type) versus *n* = 8 *Eya4*^{-/-} (knockout), with all eight showing the defect). **e**, LacZ imaging in the E12.5 *Eya4*^{+/-} revealed *Eya4* gene expression (blue) in the cochlear region (arrow). **f, g**, H&E stained histological sections through the right cochlea of an *Eya4*^{+/+} embryo (**f**) compared to an *Eya4*^{-/-} embryo (**g**) confirmed the hypoplastic phenotype. **h, i**, Higher magnification of the region (indicated by the white boxes) showed abnormal perilymphatic (periotic) mesenchyme in mutant embryos. In the mutant embryo (**i**) the perilymphatic mesenchyme did not show rarefaction and had reduced vacuolation compared to control (**h**) (arrows), suggesting that the cochlear hypoplasia was due to delayed perilymph development.



Extended Data Figure 7 | Whole brain MRI reveals many volume changes in the P7 *Tox3*^{-/-} mice. **a**, P7 *Tox3*^{-/-} knockout mouse brains were registered to an average control data set of P7 *Tox3*^{+/+} (wild-type) brains. The colours correspond to areas of larger (red) and smaller (blue) relative volumes in the knockout embryos. The colour bar minimum corresponds to a false discovery rate (FDR) threshold of 5%. Knockout mice exhibited altered volumes in multiple brain structures including an enlarged pons, amygdala and thalamus/hypothalamus and a decreased pontine nucleus when compared to the wild-type brains (arrows). Most striking was the decrease in the size of the cerebellum of the knockout mice (arrows). ($n = 8$ *Tox3*^{+/+} versus $n = 10$ *Tox3*^{-/-}, with all 10 showing the defects). Histological analysis of *Tox3*^{-/-} mice revealed abnormal

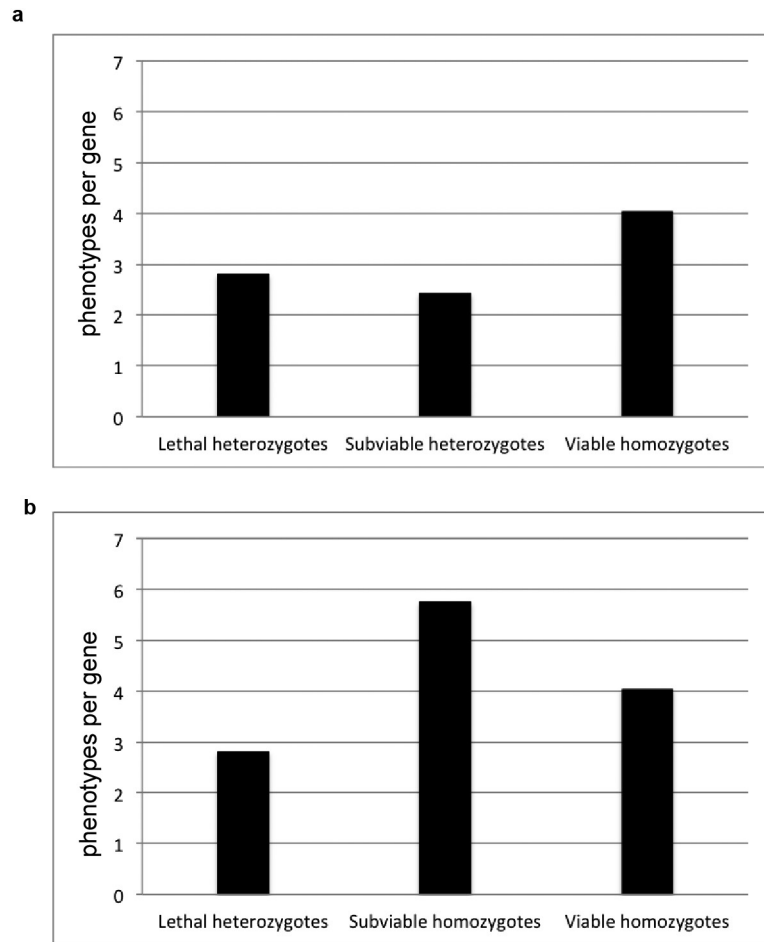


development of the cerebellum. **b, c**, The cerebellum of P7 *Tox3*^{-/-} mice is hypoplastic and dysplastic characterized by markedly reduced fissure formation, poor delineation of folia and disorganized cortical structure and layering (**c**) when compared to the P7 *Tox3*^{+/+} mice (**b**) (arrows). In some segments, there was complete absence of folial pattern. **d, e**, Higher magnification revealed that the normally transient external granular layer was absent in the *Tox3*^{-/-} mice and the subjacent molecular layer was hypotrophic and irregular in thickness and in multiple foci very thin or absent; in these foci the Purkinje cells extended to the pial surface (arrows). The Purkinje cell layer was also jumbled with no evidence of cell polarity (**e**).

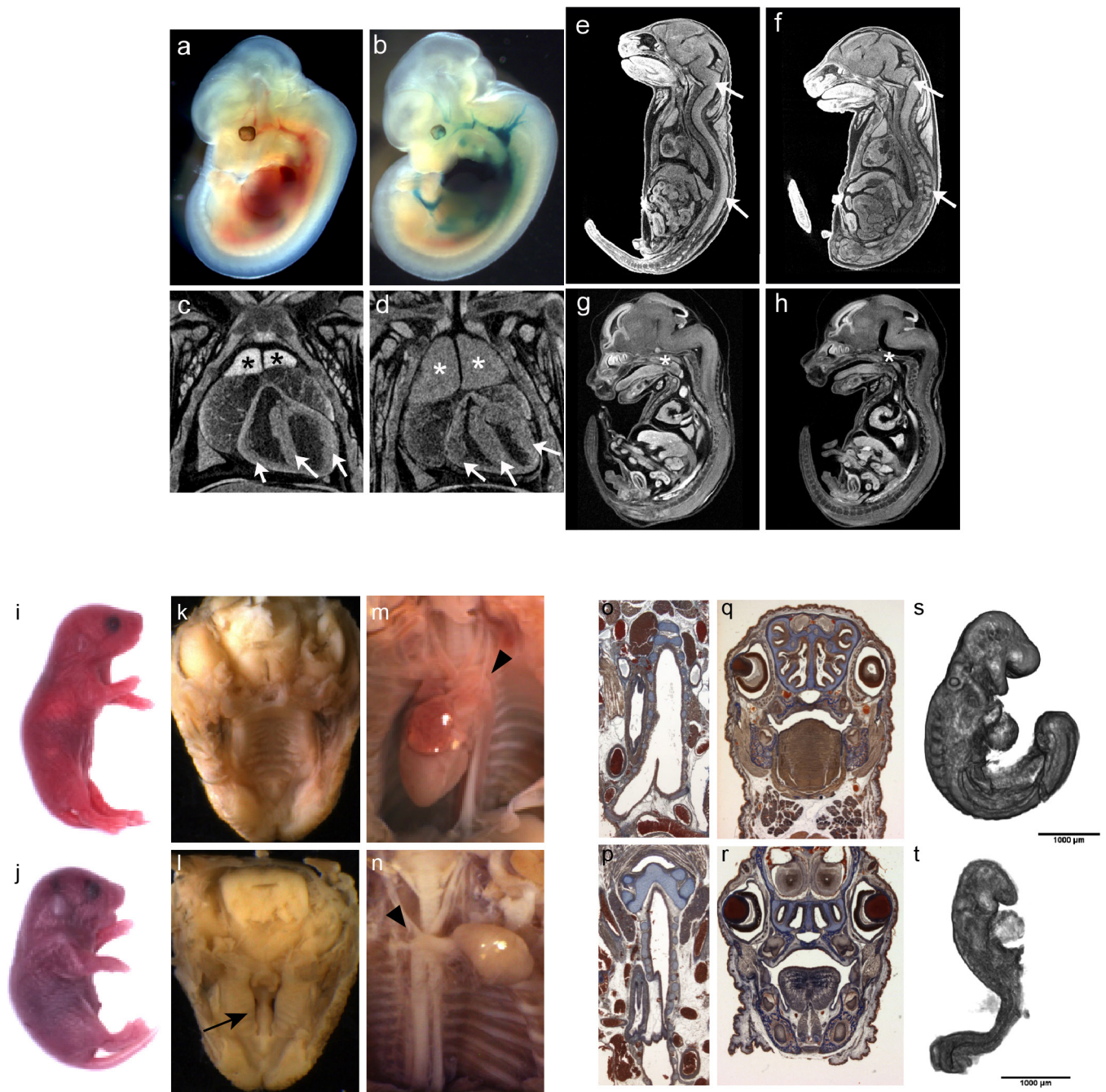


Extended Data Figure 8 | Whole brain MRI reveals enlarged ventricles in the P7 *Rsph9*^{-/-} mice. **a**, P7 *Rsph9*^{-/-} mouse brains showed enlarged left and right lateral ventricles (arrows) when virtually sectioned from rostral to caudal and compared to an average of P7 *Rsph9*^{+/+} mouse brains. ($n = 8$ *Rsph9*^{+/+} versus $n = 10$ *Rsph9*^{-/-}, with all 10 showing the defects). Histological analysis of *Rsph9*^{-/-} (knockout) mice confirmed abnormal brain development. **b**, **c**, Arrows indicate severe hydrocephalus of the left

and right lateral ventricles of the *Rsph9*^{-/-} P7 mice (**c**) compared to the *Rsph9*^{+/+} mice (**b**). The third ventricle was also enlarged but not seen in this section. **d**, **e**, Higher magnification of the cerebrum showed marked rarefaction, cavitation, and loss of periventricular cortical tissue (arrow) in the knockout mice (**e**) compared to wild type (**d**). **f**, **g**, Coronal section through the nasal region revealed that the sinuses of the knockout mice were filled with pus (asterisks) (**g**).



Extended Data Figure 9 | Phenotype hit rates from the adult phenotyping pipeline for lethal, subviable and viable lines. a, Comparison of hit rates between lethal and subviable line heterozygotes versus viable line homozygotes. **b,** Homozygous subviable cohorts showed a much higher hit rate than lethal line heterozygotes or viable line homozygotes.



Extended Data Figure 10 | Multiple phenotypes in *Gyg* and *Kdm8* null embryos. LacZ expression in *Gyg* heterozygous and homozygous embryos at E12.5 showed specific, strong expression in the heart and surrounding major vessels (that is, the dorsal aorta, the carotid artery and umbilical artery) (a, b), consistent with smooth muscle cells at this stage. Homozygous embryos were collected at expected proportions at E12.5, E15.5 and E18.5 and could not be distinguished from wild-type and heterozygous embryos by outward appearance. However, inspection of cross-sections through the whole embryo microCT images of E18.5 and E15.5 embryos showed abnormalities in several areas of the developing embryo. Thickened myocardium was evident in the hearts of 2 out of 3 homozygotes examined at E15.5 as shown in Fig. 5. Coronal cross-sections also confirmed thickened myocardium in E18.5 mutant hearts (arrows; $n = 5$ mutants), compare wild type (c) to *Gyg*^{tm1b/tm1b} (d). From the E18.5 sections, it was also obvious that the thymus was enlarged in mutants ($n = 5$ mutants) compared with controls (*), but the thymus appeared normal in E15.5 mutant embryos (data not shown). E18.5 mutant embryos also exhibited abnormal gaps in the brain and spinal cord that

we interpret as neural degeneration; compare wild-type littermates (e) to *Gyg*^{tm1b/tm1b} mutants (f) ($n = 5$ mutants). Abnormalities in the nervous system, similar to abnormalities in the heart, were obvious at E15.5. Representative images are shown from sagittal cross-sections through a wild-type (g) and a homozygous *Gyg* mutant E15.5 embryo (h) ($n = 3$). E15.5 *Gyg*^{tm1b/tm1b} mutant embryos have a flattened forebrain with reduced lateral ventricles, as well as excess space within the cephalic and cervical flexures. i–t, *Tm1a* and *tm1b* alleles can lead to phenotypes of differing strength in *Kdm8* mutants. Abnormal phenotype of *Kdm8*^{tm1a/tm1a} mice at E18.5: i, k, m, o, q, wild-type fetuses; j, l, n, p, r, mutant fetuses. i, j, gross morphological appearance of E18.5 fetuses. k–n, Photomicrographs of the palate and heart taken during necropsy. g–j, Histological sections at similar levels of the trachea and the nasal cavities, ($n = 4$ mutants analysed at E18.5). Morphology of wild-type (s) and mutants (t) *Kdm8* embryos at E9.5 captured by OPT showing developmental delay at that stage, including small size and lack of turning. Arrows, unfused palatal shelves; arrowheads, arch of the aorta. $n = 7$ mutants analysed at E9.5, scale bar = 1 mm.

Author Queries

Journal: **Nature**

Paper: **nature19356**

Title: **High-throughput discovery of novel developmental phenotypes**

Query Reference	Query
1	<p>AUTHOR: A PDF proof will be produced on the basis of your corrections to this preproof and will contain the main-text figures edited by us and the Extended Data items supplied by you (which may have been resized but will not have been edited otherwise by us).</p> <p>When you receive the PDF proof, please check that the display items are as follows (doi:10.1038/nature19356): Figs 1 (black & white); 4 (colour); Tables: None; Boxes: None; Extended Data display items: 10.</p> <p>Please check the edits to all main-text figures (and tables, if any) very carefully, and ensure that any error bars in the figures are defined in the figure legends. If you wish to revise the Extended Data items for consistency with main-text figures and tables, please copy the style shown in the PDF proof (such as italicising variables and gene symbols, and using initial capitals for labels) and return the revised Extended Data items to us along with your proof corrections.</p>
2	<p>AUTHOR: A single sentence summarizing your paper (websum), which will appear online on the table of contents and in e-alerts, has been provided below. Please check this sentence for accuracy and appropriate emphasis.</p>
3	<p>AUTHOR: Please include a scale bar for t-w, as we discussed, or include a statement like; if they are relatively normal in size 'Animals imaged in u-w were approximately 'x' mm in length from tail to snout, relatively normal for embryos of this stage' or, if they're abnormal, perhaps 'Specimens in u-w displayed abnormal growth, measuring around 'x' mm at their widest point, a marked difference from healthy embryos'; here in the legend, with 'x' modified as required.</p>
4	<p>AUTHOR: Please confirm insertion of the title.</p>
5	<p>Proofreader: Please update AOP date.</p>
Web summary	<p>Identification and characterization, using a comprehensive phenotyping pipeline, of 410 essential genes during the generation of the first 1,751 of 5,000 unique gene knockouts as part of the International Mouse Phenotyping Consortium.</p>

For Nature office use only:

Layout	<input type="checkbox"/>	Figures/Tables/Boxes	<input type="checkbox"/>	References	<input type="checkbox"/>
DOI	<input type="checkbox"/>	Error bars	<input type="checkbox"/>	Supp info	<input type="checkbox"/>
Title	<input type="checkbox"/>	Colour	<input type="checkbox"/>	Acknowledgements	<input type="checkbox"/>
Authors	<input type="checkbox"/>	Text	<input type="checkbox"/>	Author contribs	<input type="checkbox"/>
Addresses	<input type="checkbox"/>	Methods	<input type="checkbox"/>	COI	<input type="checkbox"/>
First para	<input type="checkbox"/>	Received/Accepted	<input type="checkbox"/>	Correspondence	<input type="checkbox"/>
		AOP	<input type="checkbox"/>	Author corr	<input type="checkbox"/>
		Extended Data	<input type="checkbox"/>	Web summary	<input type="checkbox"/>
				Accession codes link	<input type="checkbox"/>
				Referee accreditation	<input type="checkbox"/>

SUBJECT WORDS

Biological sciences/Genetics/Functional genomics/Mutagenesis [URI /631/208/191/1908]; Biological sciences/Genetics/Development [URI /631/208/135]; Biological sciences/Developmental biology/Experimental organisms/Model vertebrates/Mouse [URI /631/136/334/1874/345].

TECHNIQUE TERMS

Techniques: Life sciences techniques, Genomic analysis [Mutagenesis]; Life sciences techniques, Experimental organisms [Transgenic mice]; Life sciences techniques, Medical and small animal imaging [Magnetic resonance imaging]; Life sciences techniques, Experimental organisms [Mouse]; Life sciences techniques [Medical and small animal imaging]; Life sciences techniques, High throughput screening [High-throughput screening assays].